Robust Probabilities of Detection and Quantification Uncertainty for Aerial Methane Detection: Examples for Three Airborne Technologies

Bradley M. Conrad, David R. Tyner, Matthew R. Johnson*

Energy & Emissions Research Laboratory,
Department of Mechanical and Aerospace Engineering,
Carleton University, Ottawa, ON, Canada, K1S 5B6

KEYWORDS: Methane; remote sensing; aerial detection sensitivity; quantification uncertainty; monitoring, reporting, and verification; MRV; oil and gas; AMEL; Alt-FEMP; measurement-based inventories; fugitive emissions

*CORRESPONDING AUTHOR: Matthew.Johnson@carleton.ca; +1-613-520-2600 ext.4039

Abstract

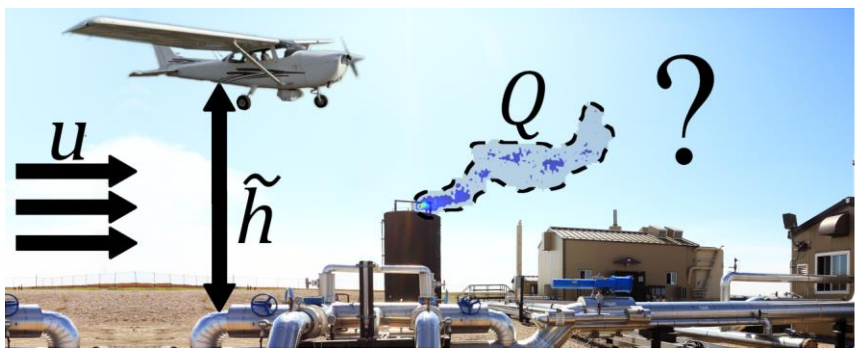

Thorough understanding of probabilities of detection (POD) and quantification uncertainties is fundamentally important when applying aerial measurement technologies as part of alternative means of emission limitation (AMEL) or alternate fugitive emissions management programs (Alt-FEMP), as part of monitoring, reporting, and verification (MRV) efforts, and in surveys designed to support measurement-based emissions inventories and mitigation tracking. This paper presents a robust framework for deriving continuous probability of detection functions and quantification uncertainty models for aerial measurement techniques based on controlled release data. Using extensive fully- and semi-blinded controlled release experiments to test Bridger Photonics Inc.'s Gas Mapping LiDAR (GML)™, as well as available release data for Kairos LeakSurveyor™ and NASA/JPL AVIRIS-NG technologies, robust POD functions are derived that enable calculation of detection probability for any given source rate, wind speed, and flight altitude. Uncertainty models are separately developed that independently address measurement bias, bias variability, and measurement precision, allowing for a distribution of the true source rate to be directly calculated from the source rate estimated by the technology. Derived results demonstrate the potential of all three technologies in methane detection and mitigation, and the developed methodology can be readily applied to characterize other techniques or update POD and uncertainty models following future controlled release experiments. Finally, the analyzed results also demonstrate the importance of using controlled release data from a range of sites and times to avoid underestimating measurement uncertainties.

Highlights

- Generalized method presented to derive aerial methane detection sensitivity
- Generalized error model also developed to derive quantification uncertainty
- Continuous probability of detection functions derived for three aerial technologies
- Results give detection probability for any source, wind, and flight altitude
- Enables use of aerial data in MRV, AMEL/Alt-FEMP, and measurement-based inventories

1 Introduction

Methane is a potent yet short-lived greenhouse gas and rapid reductions in methane emissions from energy, waste, and agriculture sectors are an essential part of the pathway to limiting global temperature rise (Arias et al., 2021; CCAC, 2021; IPCC, 2018). However, successful mitigation of emissions is contingent on the ability to reliably detect both known and unknown sources of methane. Moreover, development of trustworthy emission inventories and tracking progress toward mitigation targets requires accurate measurements within defined uncertainties. This challenge is at the heart of emerging monitoring, reporting and verification (MRV) efforts (European Commission, 2021) and the associated verification role of the United Nations International Methane Emissions Observatory (IMEO).

In recent years, a range of potential detection and/or measurement technologies have been explored with promise to significantly reduce time and labour costs to find and measure sources of methane, especially for applications in the oil and gas sector (Bell et al., 2020; Fox et al., 2019; Kemp and Ravikumar, 2021; Rashid et al., 2020; Ravikumar et al., 2019; Schwietzke et al., 2019). Of particular interest are airplane-mounted technologies which are increasingly used in large-scale field campaigns with success (Chen et al., 2022; Cusworth et al., 2021; Tyner and Johnson, 2021) and gaining acceptance in alternate fugitive emissions management programs (Alt-FEMP) replacing or supplementing optical gas imaging (OGI) surveys using hand-held infrared cameras (AER, 2021; Bridger Photonics, 2022; InvestableUniverse, 2021; Kairos Aerospace, 2022a). With sensitivities >100-1000 times better than current satellite systems, airplane-mounted sensors have emerged as a key tool for mitigating methane, well-suited to the challenging "verification" component of MRV and capable of being used to create measurement-based inventories. However, successful application of these technologies and interpretation of collected data requires a thorough understanding of the probability of detecting unknown sources under different conditions and uncertainty in quantifying emissions from detected sources. To date, only limited controlled release studies have appeared in the literature (Bell et al., 2020; Johnson et al., 2021; Ravikumar et al., 2019; Sherwin et al., 2021; Thorpe et al., 2016) and robust methodologies to meet these requirements have not been developed.

This paper has four main objectives. First, a novel generalized approach to deriving continuous probability of detection (POD) functions is presented that significantly improves upon existing formulations in the literature that are often non-physical. Generalized POD functions are essential for understanding what is or is not captured in field measurements and modelling applicability and mitigation potential of technologies in programs like FEAST (Fugitive Emissions Abatement Simulation Toolkit; Kemp et al., 2016). Second, a statistical error model is presented to derive quantification uncertainties in aerial-estimated source rates. Together with robust POD data, quantification uncertainties are essential for defensibly applying airborne measurements for MRV and ultimately for using aerial data in measurement-based inventories. Third, using extensive controlled release experiments completed to evaluate Bridger photonics' gas mapping LiDAR (GML) system (Bridger Photonics, 2021) as an initial case study, a continuous POD function and quantification uncertainty model are derived. Finally, using available published controlled release data, the methods are extended to also estimate robust POD and quantification uncertainty of Kairos LeakSurveyor™ (Kairos Aerospace, 2022b) and POD of NASA's Jet Propulsion Laboratory's Next-Generation Airborne Visible/Infrared Imaging Spectrometer (AVIRIS-NG) platform (Thorpe et al., 2016).

2 Methodology

2.1 Methane Detection Technologies

2.1.1 Bridger Photonics Gas Mapping LiDAR™

Bridger Photonics Gas Mapping LiDAR (GML) uses an airplane-mounted scanning laser, camera, and Global Navigation Satellite System – Inertial Navigation System (GNSS-INS) to detect methane sources and produce quantitative geo-located imagery of associated plumes (Bridger Photonics, 2021; Hunter and Thorpe, 2017; Johnson et al., 2021; Kreitinge and Thorpe, 2018). Originally developed through the Advanced Research Project Agency – Energy (ARPA-E) MONITOR program (ARPA-E, 2018), the technology uses wavelength modulation spectroscopy at 1651 nm to measure path-integrated methane concentrations between the aircraft and the ground, which acts as a topographic backscatterer. Forward and backward looking measurements as the plane flies give information on the detected plume height, typically within 2 m accuracy (Johnson et al., 2021). At typical target altitudes between 168 and 230 m above ground level (AGL), the sensor's 31° field-of-view results in an approximately 94–130 m wide measurement swath on the ground and resolves plumes with ~1–2 m spatial resolution. Source emission rates are estimated by a proprietary method that combines information about the spatial concentration of methane in the detected plume, the height of the plume above ground level, the horizontal wind speed at the time of detection (Bridger Photonics typically uses interpolated hourly meteorological station data provided by Meteoblue (meteoblue.com)), and the assumed vertical profile of wind speed. Preliminary analysis of blinded controlled releases by Johnson et al., (2021) suggests that 1σ quantification uncertainties of ±31–68% can be expected for sources near the sensitivity limit. However, uncertainties at higher release rates and over a broader range of conditions are not well-described in the literature and a robust understanding of these uncertainties is an important goal of this paper.

2.1.2 Kairos Aerospace LeakSurveyor™

Kairos Aerospace's LeakSurveyor is an airplane-mounted methane imaging system that combines an infrared imaging spectrometer, global positioning system (GPS) and inertial monitoring unit (IMU), and optical camera to detect methane plumes (Berman et al., 2021; Branson et al., 2021; Schwietzke et al., 2019). Path integrated methane concentrations are measured via absorption of reflected sunlight from the ground in spectral regions where there is no interference from other common hydrocarbons (Berman et al., 2021). For the targeted flight altitude of 900 m AGL, each measurement swath is approximately 800 m wide with a spatial resolution of ~3 m (Sherwin et al., 2021). As summarized in (Berman et al., 2021; Sherwin et al., 2021), quantification is via a proprietary algorithm that calculates pixel-level methane column density between the airplane and the ground, sums these estimates within a core-plume region with distinguishable methane enhancements from background, divides by the length of this core plume region, and multiplies by an estimated wind speed. Compared to Bridger Photonics' *active* GML sensor, the *passive* LeakSurveyor from Kairos Aerospace trades potential advantages of larger measurement swath permitting greater facility coverage per airplane pass with the disadvantages of lower spatial resolution and higher minimum detection limits as well as potentially greater sensitivity to environmental lighting conditions.

Because in-situ wind speed is not generally available for aircraft-detected sources and database wind speed can be highly uncertain, Kairos Aerospace typically provides source rate estimates on a wind-normalized basis – i.e., in units of emission rate per wind speed (Branson et al., 2021). Kairos' in-house (Berman et al., 2021) and third-party (Sherwin et al., 2021) assessments of the LeakSurveyor technology have estimated detection sensitivities in these units of approximately 8.2 (at a 50% POD) and 5-15 (kg/h)/(m/s) ("partial detection range"), respectively. Quantification bias was also assessed by Kairos Aerospace on wind-normalized source rate-basis and found to be approximately –2% (Branson et al., 2021); precision errors were not analyzed. In their controlled release study, Sherwin et al., (2021) independently evaluated quantification error in emission rate (non-normalized units of kg/h) by multiplying LeakSurveyor-reported wind-normalized source rate data by wind speed estimated from four different sources. The parity slope of estimated-to-controlled source rates ranged from 0.88 to 1.45×, representing a bias on the order of –12 to +45% depending on the source of wind speed data. Precision errors were estimated using the residuals of linear fits to controlled release data and were on the order of 30-42% (1σ).

2.1.3 NASA JPL's Next-Generation Airborne Visible/Infrared Imaging Spectrometer

The next-generation airborne visible/infrared imaging spectrometer (AVIRIS-NG; Hamlin et al., 2011) is an improvement on the original AVIRIS instrument (Green et al., 1998) developed by the U.S. National Aeronautics and Space Administration's (NASA) Jet Propulsion Laboratory (JPL). The AVIRIS-NG instrument is a push-broom imaging spectrometer with approximately 5 nm spectral resolution over the visible and near-infrared spectra (380 to 2510 nm). At flights altitudes relevant for methane point source detection (~400 to 3800 m AGL), the 34° field-of-view provides swath widths of approximately 250 to 2500 m with spatial resolutions of 0.4 to 3.6 m. Methane columns are retrievable using differential optical absorption spectroscopy (e.g., Thompson et al., 2015) or matched filter methods (e.g., Foote et al., 2020) permitting downstream processing to identify methane plumes.

Although the development of AVIRIS(-NG) was not specifically motivated by methane detection, AVIRIS-NG has been successfully used to detect, map, and monitor large-scale methane emitters. Methane-relevant studies have targeted measurements at an array of assorted facility types (Duren et al., 2019; Guha et al., 2020) with some focusing on oil and gas facilities (Cusworth et al., 2021; Frankenberg et al., 2016; Thorpe et al., 2020) solid waste facilities (Cusworth et al., 2020; Krautwurst et al., 2017), and arctic permafrost (Elder et al., 2020). In 2013, Thorpe et al. (2016) mounted the AVIRIS-NG instrument on a Twin Otter aircraft during controlled release experiments to evaluate methane retrieval algorithms and assess detection sensitivity as a function of wind speed and aircraft altitude; the accuracy of methane source rate estimation using AVIRIS-NG has not been evaluated at the time of writing.

2.2 Controlled Releases – Bridger GML

For this study, controlled methane releases were completed during two separate field campaigns in 2020 and 2021 at oil production sites near Lloydminster, Saskatchewan to assess Bridger Photonics' GML technology. These releases were completed as part of broader measurement surveys across western Canada and included both semi-blinded and fully blinded experiments to assess quantification accuracy as well as detection sensitivity under varying conditions. First, working collaboratively with Bridger Photonics and the contracted airplane operator, high-flowrate *semi*-blinded controlled releases were completed to derive GML quantification uncertainties when measuring methane sources emitting between 1 and 66 kg/h, consistent with 96% of sources found in a recent survey of oil and gas infrastructure in BC, Canada (Tyner and Johnson, 2021). Releases were made from a set of four inactive oil and gas facilities conveniently arranged in a line approximately 375 m apart (refer to supplemental information (SI) for additional detail). Over several days during each campaign, the plane flew laps over the test facilities while flow rates at each site were independently varied between each lap at predetermined random flow rates (including zero releases) that were not shared with Bridger Photonics.

Second, following the same approach used in (Johnson et al., 2021), additional low-flowrate controlled releases (0.4–5.2 kg/h) plus zero-releases were performed from active sites included in parallel contracted surveys of oil and gas infrastructure in the region. In collaboration with industry operators, methane was released at random rates near the expected sensitivity limit of the GML technology to test its ability to correctly detect unknown sources at unknown locations. These tests were fully blinded in that they were conducted without informing Bridger Photonics that the experiments were taking place.

At each release location time-resolved wind speed at 3 m above ground level was measured at 1 Hz using an ultrasonic wind sensor (Anemoment, TriSonica mini) with a rated accuracy of ±0.2 m/s over the relevant range of 0–10 m/s. As in (Johnson et al., 2021), after initial results were first obtained from Bridger, these in-situ wind speed data were subsequently provided to Bridger Photonics Inc., who reprocessed their results and also returned a single-valued wind speed at plume height for each flight pass and detected source. Methane from compressed cylinders (PraxAir, >99% purity) was released through Bronkhorst thermal mass flow controllers (various models, rated accuracy of ±0.1% of full scale or ±0.5% of reading). For the larger flow rates, a custom-built heated regulator and liquid-gas heat exchanger system were used to overcome Joule-Thomson cooling of the gas and ensure temperatures were near ambient as it entered the flow controllers and was subsequently released to atmosphere. At each release location, GPS-synchronized data loggers were used to record methane release rate and wind speed data that could subsequently be matched with time-stamped data provided by Bridger. This was especially important in confirming missed detections during the fully blinded releases from within sites included in the parallel surveys of oil and gas infrastructure. Table 1 summarizes the collected controlled release data.

Table 1: Summary of Controlled Release Experiments to test Bridger Photonics' GML completed as part of the present study.

Release Set	Year	Count
High-flowrate (1–66 kg/h), semi-blinded releases from a fixed set of inactive facilities[a]	2020	122 (+16 zeros)
	2021	162 (+13 zeros)
Low-flowrate (0.4–5.2 kg/h), fully blinded releases from within active sites included in parallel oil & gas sector surveys[b]	2020	67 (38 Misses)
	2021	115 (24 Misses)
Total	495 total releases	

[a] All non-zero semi-blinded releases were detected.

[b] Representative scene noise was provided with the standard data product for small-volume releases in 2020 and 2021

2.3 Available Controlled Release Data for Kairos' LeakSurveyor

Using the new methodology presented below, a robust POD function and uncertainty model were also developed for Kairos' LeakSurveyor using published controlled release data from Sherwin et al. (2021) augmented with internal controlled release data obtained from Kairos similar to (Chen et al., 2022). Sherwin et al. (2021) completed 234 semi-blinded controlled release tests of Kairos' LeakSurveyor from a single facility located in San Joaquin County, California over four days spanning October 8 to 15, 2019. These included 210 non-zero controlled releases between 18 to 1,025 kg/h. Three data points were discarded following Sherwin et al.'s (2021) initial quality control and the remaining 207 releases were used to assess detection sensitivity in the present work – 40 of these 207 releases were purposely performed at low flowrates near the lower limit of the flowmeter (<50 kg/h). Of the original 210 releases, 149 were considered for the present assessment of quantification error, corresponding to the subset of release data with a successful detection, a controlled rate > 50 kg/h, and no quality control concerns. Wind speeds were measured in situ at 8 ft (~2.43 m) above ground level using two instruments: a cup-based wind meter and a two-dimensional ultrasonic anemometer (on the latter three days only). Sherwin et al. (2021)'s analysis also evaluated quantification error for the practical scenario where in-situ wind speed data are not available, testing accuracy when using minute-resolved data from the commercial Dark Sky database (Apple Inc., 2022) and hourly data from the public High-Resolution Rapid Refresh (HRRR) database (NOAA, 2020). The LeakSurveyor sensor was used to detect and, where possible, quantify the controlled releases and was flown at a nominal altitude of 900 m AGL throughout the study. For the present analysis of POD, in-situ wind speed from the ultrasonic anemometer is favoured when available due to its improved accuracy over the cup-based meter; for the measurement day where only data from the cup-meter were available, these data are corrected based on a linear fit with available ultrasonic data. Sherwin et al. (2021) chose the one-minute gust as the representative measured wind speed (corresponding to the maximum speed during the minute prior to the aircraft overpass) in the main text of their analysis, which matches the wind speed preferred in Kairos' quantification as further discussed below. By contrast, the present analysis uses the one-minute *averaged* wind speed prior to the aircraft overpass as it is likely to be more indicative of convective dispersion of the plume prior to detection and is the relevant windspeed to consider when planning a survey or modelling expected performance in simulators like FEAST. To standardize wind speeds against the present controlled releases, all available wind data were scaled to a 3-m height AGL using a logarithmic profile with a specified zero-displacement plane, d, of 0.066 m and a surface roughness, z_0, of 0.01 m representative of the graded areas around oil and gas areas as used in Bridger's algorithm (Johnson et al., 2021).

Additional data from internal controlled release studies were provided by Kairos' to augment the present analysis of detection probabilities and quantification error. These confidential data include controlled source rate, estimated wind-normalized source rate, measured wind speed, and one-minute gust wind speed from the Dark Sky database for 375 additional non-zero releases. Within these data a total of 45 releases were missed and 296 releases were automatically detected by Kairos' algorithm; the remaining 34 were tagged as partial detects, which required human interpretation to identify a plume. When combined with the publicly available controlled release data of Sherwin et al. (2021) (which are treated as automated detects since the available data did not distinguish partial detects), there were a total of 485 detects, 34 partial detects, and 63 missed detections. Additional analysis in the SI shows the effects of treating these data sets separately. For the quantification uncertainty modelling, partial detections were not quantified, and there were total of 149–495 available source measurements depending on which wind data source was considered.

2.4 Published Controlled Release Data for NASA JPL's AVIRIS-NG

A POD function for the AVIRIS-NG sensor was derived using the controlled release data reported by Thorpe et al. (2016). These experiments were originally designed to evaluate the ability of AVIRIS-NG in detecting methane point sources and the available data do not include separate source rate estimates from the plane. A total of 143 controlled releases were completed over seven days in June 2013 from three separate sites within the Rocky Mountain Oilfield Testing Center in Wyoming, U.S.A. Thorpe et al. (2016) measured wind speeds at 8–9 m AGL using a 3D ultrasonic wind anemometer. For the present analysis of detection probability, reported wind speeds (averaged over the minute preceding a detection) were scaled from an average height of 8.5 m AGL to 3 m AGL using the same logarithmic profile and parameters noted above; the resulting wind speeds at 3 m spanned 0.66–7.5 m/s. Controlled release rates ranged from 2.2 to 96 kg/h and flight altitudes were between 430 to 3800 m AGL. For each release, the methane plume was flagged as either detected (automatic detection by algorithm, N = 94), partially detected (requiring human interpretation, N = 25), or missed (N = 24).

3 Statistical Analysis

3.1 Generalized Approach to Deriving Robust Probability of Detection Functions

For a specified remote detection technology, the probability of detection (POD) function represents the likelihood of successfully detecting an emitter at some source rate for a given set of conditions during a single measurement observation. Although different technologies may be affected by additional parameters, in general, detectability of a given source (at rate Q) depends on the wind field that drives plume dispersion, the spatial resolution of the measurement, and the effective signal-to-noise ratio (SNR) of the measurement system. For simplicity, the effects of wind can be parameterized by the measured 3-m wind speed (u_3). For Bridger's GML technology, the measured 3-m wind speed is averaged according to their algorithm and sourced directly from Bridger's reported results using the in-situ wind data at 1 Hz. For the imaging spectrometers, measured wind speed is averaged over one minute prior to the aircraft overpass to be consistent with (Sherwin et al., 2021). For a fixed set of sensor optics, the ground-level spatial resolution is defined by the altitude of the measurement system above ground level ($\tilde{h}$ [m]). The effective SNR for a given measurement is itself a function of Q and u_3 (which affect the observed path-integrated concentration of the plume), $\tilde{h}$ (which affects signal strength through the inverse square law), the spectral albedo of the ground (which affects the strength of the return signal), and potentially other parameters specific to the technology. Although additional SNR data may or may not be readily available for a given technology as further considered below, it is initially considered in this general analysis as a representative scene noise in units of column density ($\tilde{n}$ [ppm-m]). Using these parameters, a POD function can be derived that depends on $\boldsymbol{x} = \left[Q, u_3, \tilde{h}, \tilde{n}\right]^T$. Technically, the plume height ($\tilde{z}_p$) is also a relevant parameter since plume dispersion is height-dependent; however, since this is undefined for a failed detection, it is necessarily ignored in the derivation of a POD function.

A broad range of potential POD functions were evaluated using binary regression on the collected controlled release data. The objective of binary regression is to model a *discrete* binary dependent variable, here D representing a successful (1) or failed (0, "missed") detection, which follows a Bernoulli distribution. The parameter of the Bernoulli distribution is the probability of detection, i.e.,

$$D \sim Bernoulli\big(\mathrm{POD}(\boldsymbol{x})\big) \tag{1}$$

The distribution parameter $POD(\boldsymbol{x})$ is modelled via a chosen predictor function $\big(g(\boldsymbol{x};\boldsymbol{\phi})\big)$, with variables $\boldsymbol{x}$ and coefficients $\boldsymbol{\phi}$, and a *continuous* inverse link function $\big(F(g(\boldsymbol{x};\boldsymbol{\phi});\boldsymbol{\theta})\big)$, with coefficients $\boldsymbol{\theta}$:

$$\mathrm{POD}(\boldsymbol{x}) \equiv F(g(\boldsymbol{x};\boldsymbol{\phi}),\boldsymbol{\theta}) \tag{2}$$

For a candidate pair of predictor and inverse link functions, $\boldsymbol{\phi}$ and $\boldsymbol{\theta}$ are obtained by maximum likelihood estimation (MLE) of the Bernoulli distribution using controlled release data. This can be found via optimization to minimize ℓ, the negative logarithm of the likelihood function, where for the Bernoulli distribution:

$$\ell(\boldsymbol{\phi}, \boldsymbol{\theta}) = \sum_i -(D_i \ln F_i + (1 - D_i) \ln(1 - F_i)) \tag{3}$$

and $F_i = F(g(\boldsymbol{x}_i; \boldsymbol{\phi}), \boldsymbol{\theta})$ for each controlled release data point, *i*.

For a fixed probability of detection (p), the POD function may be inverted to define contours of constant sensitivity for the measurement technique. In the present case, this permits calculation of a critical source rate at some detection probability, as a function of the remaining parameters in $\boldsymbol{x}$ – i.e., $Q_p(u_3, \tilde{h}, \tilde{n}; p)$. A linear prediction model is often used in binary regression, such that $g(\boldsymbol{x}) = \boldsymbol{\phi}^T \boldsymbol{x}$, which is coupled with a logistic inverse link function (logistic regression) or a normal cumulative distribution function (CDF; probit model). However, in the present application, this approach produces lines of constant detection probability that converge to zero at zero wind ($u_3 = Q = 0$) for a fixed aircraft altitude and scene noise. This implies that an infinitesimally small emitter could be detected as wind reduces towards zero, which is non-physical for a noise-laden system. To avoid this, we allow candidate predictor functions to be nonlinear, while remaining monotonic with each element in $\boldsymbol{x}$ and non-negative (consistent with the definition of each element). Candidate predictor functions are also required to provide a non-negative output that increases with the likelihood of detection. The inverse link function maps the output of predictor function to the range [0, 1] as required.

3.2 Source Quantification Uncertainty

To interpret estimated source rate data, it is critical that measurement uncertainties are thoroughly understood. This section presents the method by which controlled release data can be used to derive predictive estimates for the true source rate (Q) given an estimated source rate ($\tilde{Q}$). Mathematically, the objective is to derive the conditional probability of Q given $\tilde{Q}$ – i.e., $\pi(Q|\tilde{Q})$. This challenge was approached by parsing observed errors during controlled release experiments into bias and precision components.

Consider hypothetical multiple detections/measurements of a single, steady-state source observed on a single, specific date. It can be assumed that, *on average*, there will be some error in the estimated value of the source rate, which represents *bias* in the measurement of this source on the specific date. A bias-correction procedure that accounts for this average error in $\tilde{Q}$ can be developed using a *bias-corrected* estimate of the source rate $\left(\hat{Q} = f_B(\tilde{Q})\right)$, which may be assumed to follow a conditional distribution $\pi(\hat{Q}|\tilde{Q})$. A *precision distribution* that accounts for precision error of the bias-corrected estimate can be similarly defined, $\pi(Q|\hat{Q})$. The desired distribution of the true source rate given the estimated source rate can then be computed from these distributions via:

$$\pi(Q|\tilde{Q}) = \int_{\hat{Q}} \pi(Q|\hat{Q})\, \pi(\hat{Q}|\tilde{Q})\, d\hat{Q} \tag{4}$$

where the integration is performed over all possible values of $\hat{Q}$. For convenience, Eq. (4) can be re-written in terms of probabilistic correction parameters κ_Q and λ_Q where $\kappa_Q = \hat{Q}/f_B(\tilde{Q})$ is a bias-correction parameter and $\lambda_Q = Q/\hat{Q}$ is a precision-correction parameter. Letting the probability distributions of these correction parameters be $\pi_{\kappa_Q}(\kappa_Q)$ and $\pi_{\lambda_Q}(\lambda_Q)$, respectively, substitution into Eq. (4) gives:

$$\pi(Q|\tilde{Q}) = \int_{\hat{Q}} \pi_{\lambda_Q}\left(\frac{Q}{\hat{Q}}\right) \pi_{\kappa_Q}\left(\frac{\hat{Q}}{f_B(\tilde{Q})}\right) \frac{1}{\hat{Q} f_B(\tilde{Q})}\, d\hat{Q} \tag{5}$$

Since bias-correction accounts for the average error in $\tilde{Q}$, the parameters of the precision-correction distribution $\left(\pi_{\lambda_Q}\right)$ must be chosen to yield a unit mean. Likewise, the parameters of the bias-correction distribution $\left(\pi_{\kappa_Q}\right)$ can be constrained to have a unit mean while optimizing for the coefficients of the bias-correction function (f_B).

There is one simplifying limiting case for the conditional distribution shown in Eq. (5) that is necessary if controlled release data are constrained to a small set of sites and/or measurement days. In this case, measurement error must be assumed to be *independent* of time and location, implying that the required bias-correction is non-probabilistic. With this assumption, Eq. (4) simplifies to:

$$\pi(Q|\tilde{Q}) = \pi_{\lambda_Q}\left(\frac{Q}{f_B(\tilde{Q})}\right) \frac{1}{f_B(\tilde{Q})} \tag{6}$$

The conditional probability distributions in Eq. (6) were computed via MLE using controlled release data for Bridger's GML and Kairos' LeakSurveyor technology. This approach optimizes the parameters for π_{λ_Q} (constrained to yield a unit mean) and the coefficients of the bias-correction function, f_B.

Myriad other parameters could influence error in source rates estimated from aerial measurements. These include the time-history of the turbulent wind field over the site as well as parameters impacting the quality of the measurement signal (e.g., aircraft altitude/orientation and surface albedo). In the most general sense, the desired probability distribution(s) should be conditioned on these additional parameters. However, error caused by these parameters are likely to be highly site-, source-, and time-dependent, such that these confounding variables are inherently considered if extensive controlled release data for multiple sites over multiple days are available and Eq. (5) can be used to model quantification error. Conversely, since Eq. (6) assumes errors are independent of site, source, and time, this latter model can be expected to underestimate variance in the quantification error. This is further explored in Section 4.2.1 below.

4 Results

4.1 Probability of Detection

Starting first with the detailed case-study of Bridger's GML, Figure 1a plots the 466 non-zero controlled releases obtained during the 2020 and 2021 campaigns as a function of measured 3-m wind speed. Successful detections of fully and semi-blinded releases are identified in blue and green, respectively, and misses in red. There were no false positives during the 29 zero controlled releases. Over this range of wind speeds between 0.5 and 7.2 m/s, all sources greater than ~4.5 kg/h were detected. Figure 1b shows a magnified view of the same data for source rates less than 8 kg/h, which highlights the probabilistic nature of detection success.

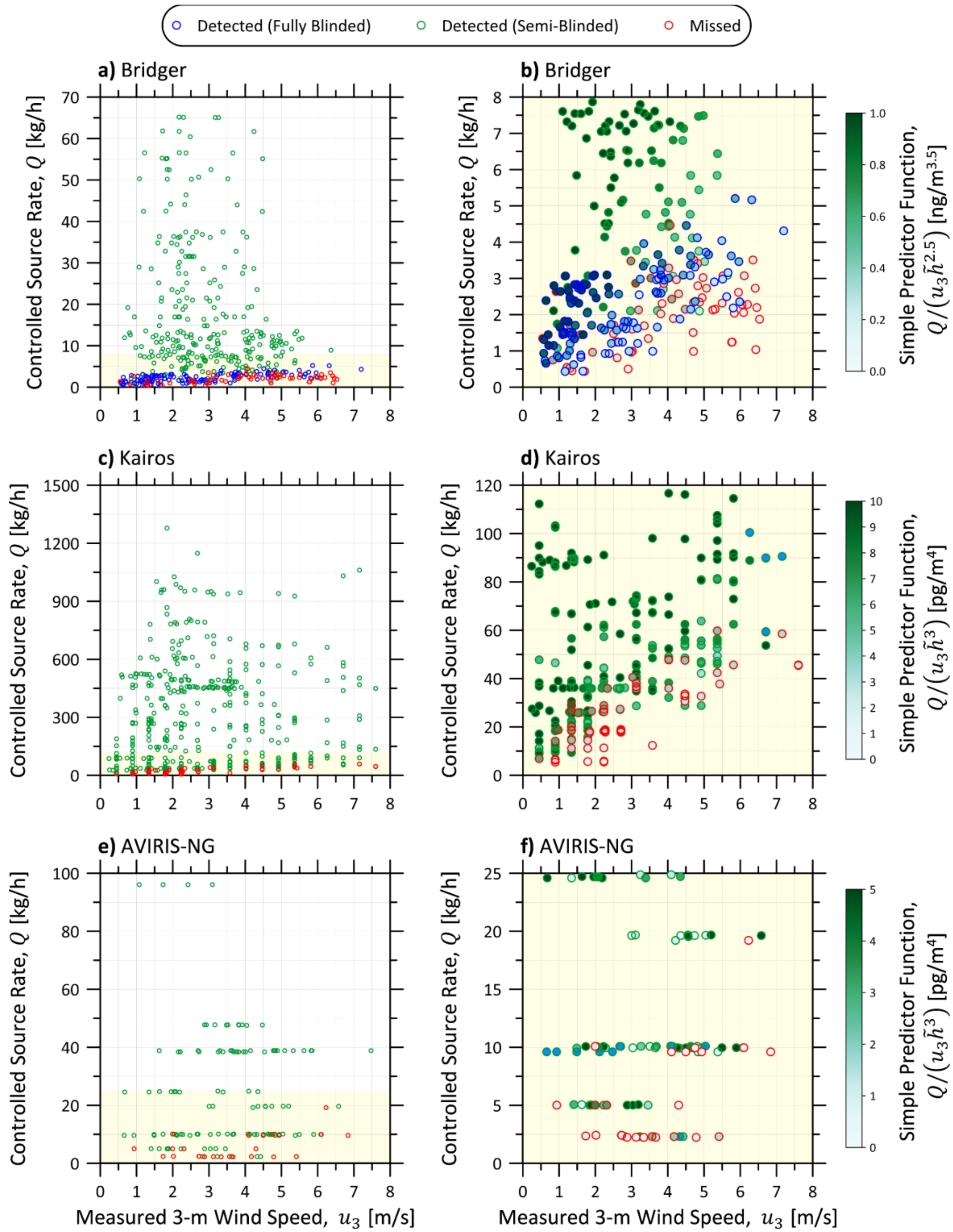

Figure 1: Available controlled release data for (a,b) Bridger Photonics GML, (c,d) Kairos LeakSurveyor, and (e,f) AVIRIS-NG. Successful detections are outlined in blue (fully blinded data) or green (semi-blinded data) and missed detections are outlined in red. Righthand panels (b, d, and f) show a zoomed subset of lower release rate data from the corresponding left panels, where the data points are also shaded according to each technique's simple predictor function (described in the main text) as outlined on the right of each panel.

Expectedly, successful detection appears more likely at higher source rates and lower wind speeds – i.e., detection probability is correlated with the wind-normalized source rate as in previous studies (e.g., Sherwin et al., 2021). This is anticipated by the simplified Gaussian plume dispersion model (Hanna et al., 1982), where the wind-normalized source rate is proportional to the plume column density along the vertical axis (i.e., the observable "signal" for an airborne measurement). However, detection is also affected by the strength of the return signal at the optics which is proportional to $\tilde{h}^{-2}$ (inverse square law) and the spatial resolution of the imagery, which for Bridger's scanning laser and GML optics is approximately proportional to $\tilde{h}^{-0.5}$. Including these effects, while still ignoring the effect of instrument noise for the time-being, provides an informative, non-parametric, *simple* predictor function for Bridger's GML, $g(\boldsymbol{x};\boldsymbol{\phi}) \approx \frac{Q}{u_3\tilde{h}^{2.5}}$. This function is used to colour the data in Figure 1b, scaled to units of ng/m$^{3.5}$. Visually, the colour gradient in the data from the top-left (high detection probability) to the bottom right (low detection probability) suggests strong correlation of this simple predictor with detectability.

Similar data are shown for the Kairos LeakSurveyor (Figure 1c-d) and AVIRIS-NG (Figure 1e-f) instruments. In contrast to Bridger's GML with actively scanning optics, the detection sensitivity of these passive imaging spectrometers is expectedly lower, such that some emissions likely to be detected by Bridger may be missed by Kairos' LeakSurveyor or AVIRIS-NG. Additionally, for these imaging optics that can be approximated with a pinhole model, spatial resolution at the ground/plume is linear with aircraft altitude, such that the equivalent *simple* prediction function these techniques should be $g(\boldsymbol{x};\boldsymbol{\phi}) \approx \frac{Q}{u_3\tilde{h}^3}$, indicating a greater sensitivity to aircraft altitude than Bridger's GML. Figure 1d and f show the controlled release data according to this latter predictor function in units of pg/m^4 – recall however, that available Kairos data were acquired at the single targeted altitude of 900 m AGL. Interestingly, in contrast to Bridger's GML, the gradient in this colouring scheme is less pronounced for AVIRIS-NG, indicating that detection sensitivity is not well-captured by the simple predictor model.

Although potentially useful, the simple predictor functions $g(\boldsymbol{x};\boldsymbol{\phi}) \approx \frac{Q}{u_3\tilde{h}^{2.5}}$ and $g(\boldsymbol{x};\boldsymbol{\phi}) \approx \frac{Q}{u_3\tilde{h}^3}$ in Figure 1b, d, and f are sub-optimal since, in addition to being non-parametric and approximate, this formulation forces contours of constant POD to be linear and converge at the origin in the Q-u_3 domain. Thus, for a fixed aircraft altitude, this formulation results in the same non-physical POD at low wind speeds as the linear predictor model. To avoid this issue and to generalize the predictor model, the present analysis considers an optimizable model of the form:

$$g(\boldsymbol{x};\boldsymbol{\phi}) = \phi_7 \frac{\left(Q_{[\mathrm{kg/h}]} - \phi_1\right)^{\phi_3}}{\tilde{n}_{[\mathrm{ppm \cdot m}]}^{\phi_4} \left(\frac{h_{[\mathrm{m}]}}{1000}\right)^{\phi_5} \left(u_{3\left[\frac{\mathrm{m}}{\mathrm{s}}\right]} - \phi_2\right)^{\phi_6}} \tag{7}$$

where representative scene noise ($\tilde{n}$) has been introduced for completeness and may be optionally considered via optimization of coefficient ϕ_4 and units of each variable have been explicitly stated in square brackets. Choosing $\phi_1 > 0$ and/or $\phi_2 < 0$ ensures a physically reasonable POD at zero-wind, unlike the linear prediction model and the simple, non-parametric predictor functions described above and used to colour data in Figure 1b, d, and f. Similarly, non-negative exponents ϕ_{3-6} allow for deviation from linearity or, in the case of ϕ_5 for aircraft altitude, from the expected value of 2.5 (GML) or 3.0 (LeakSurveyor and AVIRIS-NG). Importantly, the generalized predictor model of Eq. (7) is non-negative and monotonically increases with source rate and decreases with scene noise, aircraft altitude, and 3-m wind speed. This means that candidate inverse link functions can take the form of the cumulative distribution function (CDF) of any distribution with non-negative support (e.g., lognormal, Fréchet, etc.).

As further detailed in the SI (see especially Table S1), the optimization considered a broad range of possible inverse link functions while independently testing the importance of each variable in Eq. (7). Considering first the subset of controlled release measurements where scene noise data were available, in all instances the optimization showed that including either scene noise *or* aircraft altitude in the model, i.e., permitting ϕ_4 *or* ϕ_5 to be non-zero, was strongly statistically justified. By contrast, including both parameters was either not justified or only marginally justified ($\Delta AICc < \sqrt{10}$, see SI); that is, classed as "not worth more than a bare mention" (Kass and Raftery, 1995; Snipes and Taylor, 2014). Thus, given that aircraft altitude is a trivial parameter to quantify (and in the present case available for Bridger's GML as a standard output), the remainder of the POD derivation ignores scene noise, forcing $\phi_4 = 0$ and optimizing for the exponent on aircraft altitude, ϕ_5.

Subsequent optimization was performed using all available controlled release data plotted in Figure 1a for Bridger's GML (N = 466), Figure 1c for Kairos' LeakSurveyor (N = 207), and Figure 1f for AVIRIS-NG (N = 139). As an example, the best-fitting model for the GML data had the following optimized predictor function:

$$g(Q, u_3, \tilde{h}) = \frac{0.1518\ Q_{[\mathrm{kg/h}]}^{1.072}}{\left(\frac{\tilde{h}_{[\mathrm{m}]}}{1000}\right)^{2.440} \left(u_{3[\mathrm{m/s}]} + 2.139\right)^{1.692}} \tag{8}$$

and employed a Fréchet CDF for the inverse link function:

$$F(g) = \exp(-0.3719 g^{-2.530}) \tag{9}$$

Combined, these give the probability of detection for any specific source rate, wind speed, and altitude using Bridger's GML. Importantly, the generalized approach used to produce this detailed model can be readily extended to any other technology for which sufficient controlled release data are available. Using published controlled release data for Kairos' LeakSurveyor (Sherwin et al., 2021) and AVIRIS-NG (Thorpe et al., 2016), POD functions were derived for each of these technologies using the developed method. The composite POD functions joining the predictor and inverse link are summarized for each technology in Table 2; optimized coefficients for the predictor functions are available in the SI. For both Kairos' LeakSurveyor and AVIRIS-NG cases, representative instrument noise data for the controlled releases were not available (hence, $\phi_4 = 0$). Additionally, for Kairos' LeakSurveyor, aircraft altitude was constant during controlled release experiments so the optimized exponent on aircraft altitude (ϕ_5) was also necessarily ignored. Coefficients of the optimized predictor and inverse link functions for each measurement technology are summarized in Table 2.

Table 2: Derived POD functions for GML, LeakSurveyor, and AVIRIS-NG, combining optimized predictor and inverse link functions. Detailed equations of the predictor and inverse link functions for each technology are summarized in Table S3 of the SI.

Technology	**Optimized Probability of Detection (POD) Function**
Bridger Photonics Inc. Gas-mapping LiDAR (GML)	$\mathrm{POD} = \exp\left(-\left(\frac{0.2244\, Q_{[\mathrm{kg/h}]}^{1.072}}{\left(\frac{\tilde{h}_{[\mathrm{m}]}}{1000}\right)^{2.440}\left(u_{3[\mathrm{m/s}]}+2.139\right)^{1.692}}\right)^{-2.530}\right)$
Kairos Aerospace LeakSurveyor	$\mathrm{POD} = 1-\left(1+\left(\frac{\left(5.266\times10^{-3}\right) Q_{[\mathrm{kg/h}]}^{2.054}}{\left(u_{3[\mathrm{m/s}]}+0.9296\right)^{2.056}}\right)^{1.303}\right)^{-3.906}$
Including Partial Detections	$\mathrm{POD} = 1-\left(1+\left(\frac{\left(2.116\times10^{-3}\right) Q_{[\mathrm{kg/h}]}^{2.027}}{\left(u_{3[\mathrm{m/s}]}+0.07006\right)^{1.527}}\right)^{1.303}\right)^{-3.906}$
NASA JPL AVIRIS-NG	$\mathrm{POD} = 1-\left(1+\left(\frac{\left(5.613\times10^{9}\right) Q_{[\mathrm{kg/h}]}^{2.431}}{\left(\frac{\tilde{h}_{[\mathrm{m}]}}{1000}\right)^{1.684}\left(u_{3[\mathrm{m/s}]}+36.44\right)^{7.643}}\right)^{1.303}\right)^{-3.906}$
Including Partial Detections	$\mathrm{POD} = \exp\left(-\left(\frac{\left(3.141\times10^{6}\right) Q_{[\mathrm{kg/h}]}^{1.101}}{\left(\frac{\tilde{h}_{[\mathrm{m}]}}{1000}\right)^{0.7343}\left(u_{3[\mathrm{m/s}]}+37.11\right)^{4.420}}\right)^{-2.530}\right)$

[a] Aircraft altitude during controlled release experiments of Kairos' LeakSurveyor did not deviate from the targeted aircraft altitude of 900 m AGL (approximately 3000 ft), so aircraft altitude is necessarily ignored in the stated POD function. The optimized model can theoretically be extended to other altitudes by forcing the exponent on aircraft altitude to its expected value of 3.0 and updating other coefficients as necessary. Note however that there are no public data to support model accuracy at other altitudes and this extrapolation should be performed with caution given the observed deviation of AVIRIS-NG's optimized predictor function from the same expected value of 3.0.

Optimization of the generalized predictor function in Eq. (8) using the controlled release data for Bridger's GML technology identified an optimal exponent on aircraft altitude (ϕ_5) of 2.440, quite close to the theoretical/expected value of 2.5. By contrast, optimization of the AVIRIS-NG controlled release data yielded an optimal exponent on aircraft altitude of 0.7373−1.684, which is lower than the expected value of 3.0 assuming simple pinhole optics. Given this deviation and noting that aircraft altitude was not varied from the targeted level in the controlled release studies of Kairos' Leak Surveyor, one should use caution if seeking to extrapolate from the presented POD function for Kairos to other altitudes.

Figure 2a-c plots detection success against the value of the optimized predictor function for the controlled releases of Bridger's GML, Kairos' LeakSurveyor, and AVIRIS-NG, respectively. The optimized inverse link function is overlaid in each plot. Figure 2d-f combines the optimized predictor and inverse link to display the POD function within the Q-u_3 domain at typical aircraft altitudes for Bridger's GML (175 m), Kairos' LeakSurveyor (900 m), and AVIRIS-NG (1300 m, Thorpe et al., 2016), respectively. Contours at probabilities of detection of 10, 50, and 90% – and the associated functions, Q_p – are also plotted as solid green lines. The dashed green lines (and associated functions, Q'_p) show the POD if partial (human-identified) detections are included in the analyses of Kairos' LeakSurveyor and AVIRIS-NG and treated equally as algorithmic detections.

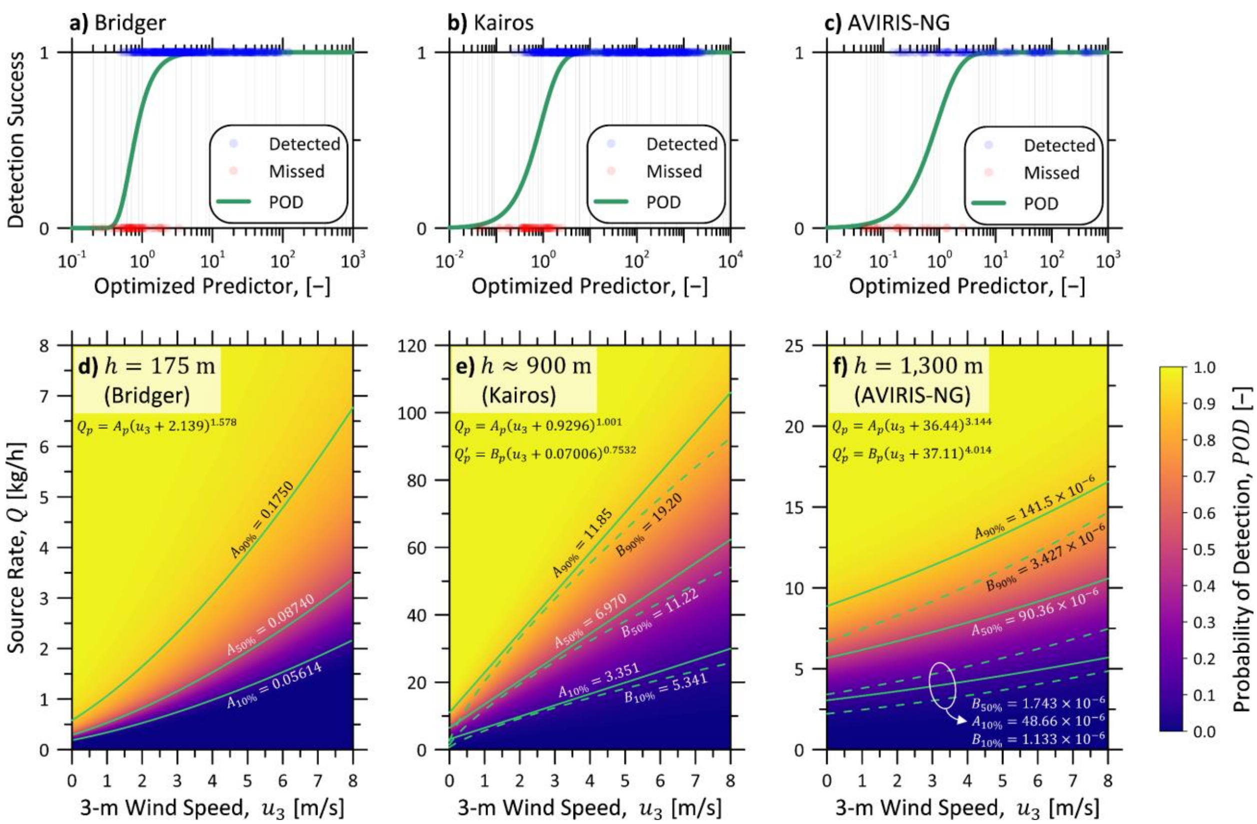

Figure 2: Robustly derived probability of detection (POD) functions for Bridger's GML technology, Kairos' LeakSurveyor technology, and AVIRIS-NG. a-c) detection success against optimized predictor function values for all available controlled release data for each instrument alongside the corresponding optimized inverse link function (green line). d-f) calculated probability of detection as a function of source rate and 3-m wind speed at typical flight altitudes for each instrument. Contours for probabilities of detection of 10, 50, and 90% and their associated functions (Q_p) are overlaid in each plot as solid green lines. For comparison, POD contours if partial detections are included are also plotted with their associated functions (Q'_p) as dashed green lines. Table 2 provides general equations for POD as a function of source rate, wind speed, and altitude (where relevant) for all cases in this figure.

The POD functions plotted in Figure 2d-f and summarized in Table 2 provide continuous detection probabilities on a *measurement-specific* basis for any given wind speed, source rate, and altitude. These functions have not existed to date and are precisely what is required for realistic analysis using emissions abatement simulators like FEAST (Kemp et al., 2016) and modelling efforts supporting alt-FEMP applications. In FEAST for example, detection sensitivity has to date been treated as a binary variable with successful detection assumed if an instrument's sensitivity is exceeded by the maximum plume concentration estimated from Gaussian plume dispersion theory. This approach inherently ignores the continuous nature of detection probability and assumes idealized plume dispersion that is not supported by the data. The continuous POD functions developed in this work identify non-linear sensitivities to source rate size and measurement conditions and can be readily implemented within FEAST and other models to probabilistically assess detection success. Similarly, robust POD data are vital for objective analysis of missed detections in situations where multiple measurements are made over the same facility.

As expected and noting the different scales in Figure 2d-f, the detection sensitivities of Bridger's active sensor are much lower than either of the passive sensors. Considering typical altitudes of 175, 900, 1300 m for each technology respectively, at a common reference wind speed of 3 m/s, Bridger's GML can be expected to detect a 1.2 kg/h source at 50% probability, Kairos a 26/27 kg/h source, and AVIRIS-NG a 4.7/7.3 kg/h source (the latter two lower/upper values depending on whether partial, human-reviewed detections are considered as detections or not). At fixed altitudes, the optimized POD functions for all three technologies provide physically realistic non-zero intercepts at zero wind speed. These contours contrast with assumed detection sensitivities or partial detection ranges with non-physical zero-intercepts based on wind-normalized source rates for Kairos' LeakSurveyor (Berman et al., 2021; Chen et al., 2022; Sherwin et al., 2021) as well as the assumed linear model of Johnson et al. (2021) for Bridger's GML. Figure S2 of the SI compares the newly derived continuous POD functions with these previously published detection sensitivities for each technology. There is a slight improvement in the detection sensitivity of Bridger's GML over that estimated from limited tests in the 2019 data of (Johnson et al., 2021). Detection sensitivities are of similar magnitude for Kairos' LeakSurveyor as in Sherwin et al.'s (2021) and Berman et al.'s (2021) analyses. Likewise, the present approach overlaps significantly with Thorpe et al.'s (2016) stated partial detection range, however the new result improves upon this by parameterizing the POD with wind speed and altitude aircraft.

The optimized POD function for Kairos' LeakSurveyor is approximately linear with wind speed. While this result is justified by goodness-of-fit statistics, subjective inclusion/exclusion of data can yield significantly different results. Using this technology as an example and referring to Figure S3 in the SI, POD contours are super-linear if Sherwin et al.'s (2021) data are considered alone (Figure S3a) but, by contrast, become sub-linear if only Kairos' internal data are considered (Figure S3b). Only when combining these unique data sets does the optimized POD function yield contours that are approximately linear (Figure S3c). This sensitivity to data inclusion is likely due to the scarcity of data near the sensitivity limit in

Sherwin et al.'s (2021) experiments (see Figure S3a in the SI). For instance, one-minute-averaged 3-m wind speeds during Sherwin et al.'s (2021) experiments did not exceed 5.5 m/s as compared to maximum wind speeds of 7.4 m/s in the Bridger GML and >8.0 m/s in the AVIRIS-NG controlled release data. Moreover, due to instrumentation constraints noted by Sherwin et al. (2021), releases near the sensitivity limit were occasionally held constant during consecutive (up to 16) flight passes, letting the variable wind perturb detectability of the plume. Consequently, the available controlled release data tend to be clustered in the Q-u_3 domain, such that a POD function for Kairos' LeakSurveyor derived from Sherwin et al.'s (2021) data alone should not be extrapolated. Nevertheless, the observed sensitivity of the optimized POD function to the contributing datasets supports the continued acquisition (and public sharing) of controlled release data for these technologies.

As presented, the derived POD assumes accurate knowledge of aircraft altitude and 3-m wind speed. This is the appropriate form when trying to understand what might be detectable in a range of field study scenarios and/or modelling of alternate fugitive emissions management programs (Alt-FEMP) or alternative means of emission limitation (AMEL) proposals. However, when interpreting data from a specific field campaign, accurate in-situ wind data are generally not available and database/modelled wind speed must instead be used to infer the POD. This scenario necessarily requires an error model for the wind speed. Such a model is likely to be highly dependent on time and location as well as the source of the wind speed estimate and ideally should be derived from data relevant to any particular measurement campaign. However, if a wind error model of the form $\pi(u_3|\tilde{u}_3)$ exists (i.e., a conditional distribution of the true 3-m wind speed given the available estimate), then the POD can be readily quantified considering bias/precision in the estimated 3-m wind speed via:

$$\mathrm{POD}\left(Q,\tilde{u}_3,\tilde{h}\right) = \int_0^\infty \mathrm{POD}\left(Q,u_3,\tilde{h}\right)\pi(u_3|\tilde{u}_3)du_3 \tag{10}$$

To enable this type of analysis, wind speed error distributions, $\pi(u_3|\tilde{u}_3)$, were derived using available wind data from the controlled release trials of Bridger's GML and Kairos' LeakSurveyor. The resulting distributions are summarized in Table S5 of the SI and can be used with the optimized POD functions in Table 2 to compute probabilities of detection given *estimated* wind speed via Eq. (10).

4.2 Measurement Uncertainty

Figure 3 compares the known (Q) and estimated ($\tilde{Q}$) source rates across the controlled release studies of Bridger's GML and Kairos' LeakSurveyor technologies. Estimated source rates for Bridger's GML technology were taken directly from their reported results; all 284 non-zero, semi-blinded, high-flowrate releases in the 2020 and 2021 campaigns are shown in Figure 3a alongside a 1:1 parity line. Figure 3b plots similar data from Sherwin et al.'s (2021) controlled release experiments of Kairos' LeakSurveyor. The 149 data points in this latter case correspond to all controlled releases greater than 50 kg/h and without any identified quality control concerns. Source rates were computed from Kairos' estimated wind-normalized source rates and multiplied by modelled wind speed at 3-m height above ground. Four datasets are shown in Figure 3b corresponding to wind data from Dark Sky – one-minute average (green) and gust (yellow) – and HRRR – one-hour average (red) and gust (blue). Figure 3c plots the resulting probability distributions for the relative error ratio ($\mathrm{RER} = Q/\tilde{Q}$) from the data in Figure 3a and b according to Eq. (6), which ignores potential site-to-site and day-to-day variability in measurement accuracy; means of each distribution, representing overall measurement biases, are identified by points. Bridger's GML estimates using Meteoblue wind data and Kairos' LeakSurveyor estimates using one-minute *gust* data from Dark Sky show minimal bias errors, with relative error ratios of 0.95 and 1.04, respectively. By contrast, bias errors can be large (1.34) when using one-hour gust wind data from HRRR and prohibitively large using one-minute *average* Dark Sky or one-hour *average* HRRR data (2.14 and 2.53, respectively) with Kairos' LeakSurveyor technology. Table 3 summarizes key statistics (mean, median, and 95% equal tail distributions) for each of these distributions shown in Figure 3c and Table S4 of the SI provides detailed equations for the conditional probability distribution, $\pi\left(Q\middle|\tilde{Q}\right)$, for each combination of technology and wind speed data source. These distributions are the essential inputs for Monte Carlo methods enabling comprehensive uncertainty analysis in large measurement campaigns (e.g., Tyner and Johnson, 2021), which may include multi-pass measurements of single sources/facilities, and specifically include aggregation of detected sources to develop measurement-based inventories.

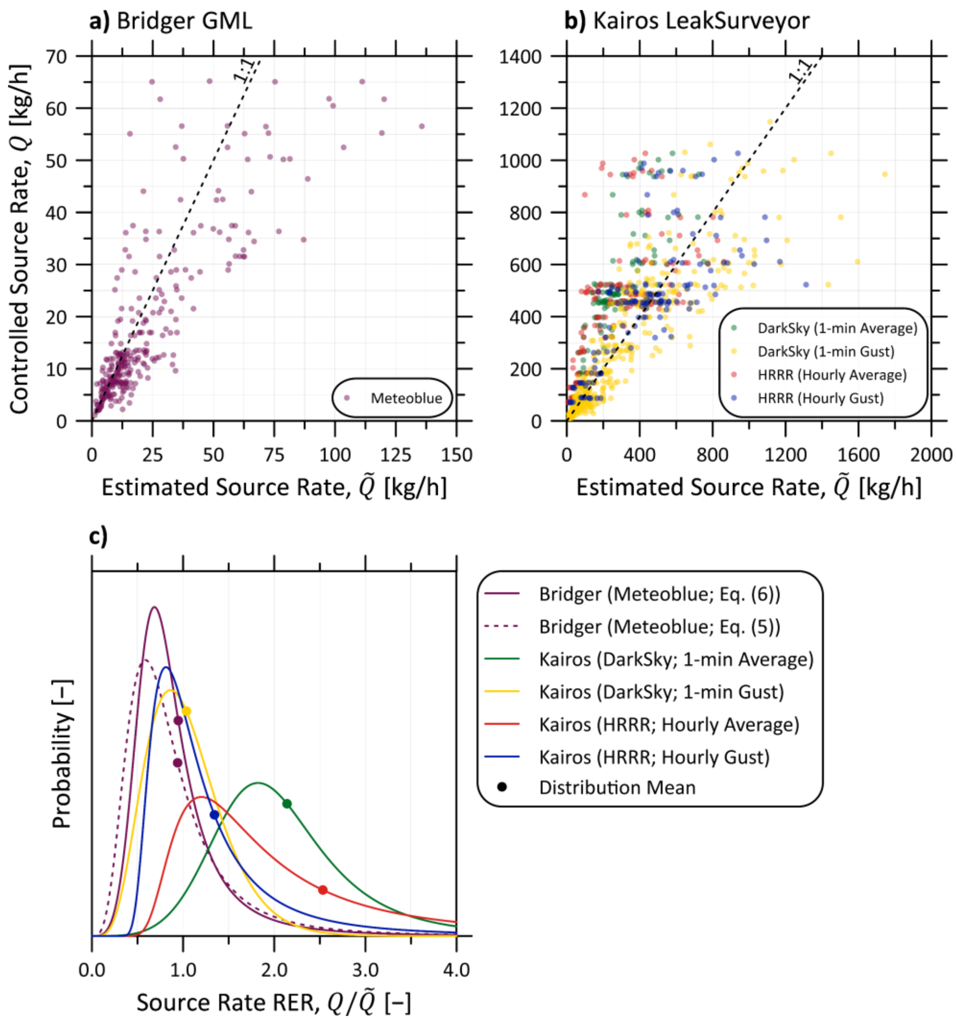

Figure 3: Summary of controlled release data and quantification error analysis for a) Bridger's GML technology using Meteoblue wind data (purple) and b) Kairos' LeakSurveyor technology, computed using Dark Sky one-minute average (green) and gust (yellow) and HRRR hourly average (red) and gust (blue) wind data. (c) Resulting distributions of the source rate relative error ratio (RER) for each technique and wind source via fitting of Eq. (6) in addition to the source rate RER for Bridger's GML technology using Eq. (5). Distribution means, representing quantification bias error are identified for each distribution by a point.

Table 3: Statistics of the relative error ratio (RER = $Q/\widetilde{Q}$) for Bridger's GML and Kairos' LeakSurveyor technologies; source data corresponds to the high-flowrate (1-66 kg/h) controlled releases from the present study and all valid controlled releases > 50 kg/h from Sherwin et al. (2021). RER statistics (mean, median, and 95% equal tail confidence interval (CI)) are shown for each technique and, for Kairos' LeakSurveyor, when using different sources of wind speed data.

Instrument	Wind Source	Wind Statistic	Mean (Bias)	Median	95% Equal Tail CI
Bridger GML	Meteoblue	Proprietary	0.95	0.81	0.35 – 2.41
Kairos LeakSurveyor	Dark Sky	1-min Gust	1.04	0.98	0.38 – 2.02
		1-min Average	2.14	1.99	0.93 – 4.27
	HRRR	1-hr Gust	1.34	1.06	0.56 – 3.81
		1-hr Average	2.53	1.75	0.77 – 8.82
	In Situ	1-min Gust	0.98	0.91	0.43 – 1.92
		1-min Average	1.39	1.28	0.58 – 2.85

The improved quantification accuracy when using *gust* instead of *average* wind speeds to estimate source rate with Kairos' LeakSurveyor is somewhat counterintuitive since average wind speed is more indicative of the history of plume propagation prior to any observation. This seemingly anomalous observation could be a result of the coarse spatiotemporal resolution in database/modelled winds, which might tend to underestimate averages of non-negative and right-skewed wind speeds. However, this is much more likely related to how Kairos' wind-normalized source rate is estimated based on a defined "core" of the plume. Specifically, Kairos estimates wind-normalized source rate by dividing the total observed excess methane mass in the "core" of the plume by the length of this plume "core" in the direction of the wind; to then estimate source rate, this parameter is multiplied by the estimated wind speed. This is equivalent to averaging the flux of methane through control surfaces orthogonal to and spanning the length of the plume core. This approach is only valid in the case of infinite sensitivity where excess methane at the edges of the plume is fully resolved. In practice though, finite sensitivity implies that the excess mass of methane in the plume is inherently underestimated, and this effect is accentuated by constraining the analysis to an arbitrary plume core. To overcome this underestimation of plume mass, an upward correction to wind speed would be necessary. This same result has been identified for satellite-based methane detection methods – particularly the cross-sectional flux (CSF) method (e.g. Varon et al., 2018 and references therein), which is similar to Kairos' approach. Robust analyses of this quantification method in the context of satellite remote sensing confirms that database/modelled average wind speeds must be calibrated/corrected to accurately recover known source rates. The calibration correction has been found to be sensor noise- and plume-dependent and studies have estimated it to range from +30 to +75% for satellite instruments (Jervis et al., 2021; Varon et al., 2020). Recognizing that database/modelled wind speeds are inherently biased and uncertain, it is possible and perhaps likely that the upward correction used to estimate gust wind speed from an average wind speed tends to mimic this required calibration correction.

To explore this further, Table 3 shows RER statistics for Kairos' LeakSurveyor using in-situ wind speed data from Sherwin et al. (2021) and Kairos' internal controlled release studies. One-minute-averaging of in-situ wind speed tends to underestimate the true source rate (RER of 1.39), corresponding to a +39% calibration correction needed to minimize bias; this is consistent with published corrections needed for satellite imagery using the CSF method (Jervis et al., 2021; Varon et al., 2020). However, the in-situ, one-minute gust wind speed compensates for this underestimation (RER of 0.98). Thus, in this specific example, if wind-normalized source rate is derived using Kairos' plume "core", then the one-minute gust wind speed empirically minimizes bias.

4.2.1 Spatiotemporal Variability of Measurement Bias

Use of the simpler error model shown in Eq. (6) assumes that site-to-site and day-to-day bias in measurement error for a given technique is negligible. While this is a necessary assumption if controlled release data are limited to few locations/days, it is also uncertain. For example, drift in optical components and general atmospheric conditions may influence day-to-day variability in quantification accuracy, while localized conditions such as wind direction/turbulence and ground albedo can affect site-to-site variability. To glean insight into this bias variability, an additional analysis was performed using the present controlled release data for Bridger's GML technology, which includes releases from four oil and gas sites recorded over multiple days in two field campaigns one year apart. Figure 4a presents a box-whisker diagram for the relative error ratio (RER) of the Bridger GML-estimated source rate, which takes the 284 controlled releases and computes statistics for data aggregated by measurement day (eight days spanning 2020 and 2021) and site (four locations). In these diagrams the central bar represents the interquartile range (25^{th} to 75^{th} percentile), the gray bars extend to the 90% equal tail confidence interval (CI), and the red crosses indicate extreme data outside the 90% CI. The central bars are notched at the mean value of the aggregated data, which represents bias for a specific measurement day or location. Measurement bias (quantified as the mean source rate RER at a particular site or on a particular measurement day) varied moderately on a site-by-site basis, from 0.89 to 0.99, and significantly on a day-to-day basis, from 0.53 to 1.74. This implies that bias on any one day and/or at any one site can be significant; however, available data also imply that, on average, bias across multiple days/sites is not statistically different than unity at a 5% significance level.

Figure 4b provides insight into the source of bias variability by showing the same box-whisker diagrams for the RER in modelled 3-m wind speed from Meteoblue (used in Bridger's quantification) vs. the actual measured wind speed. As evidenced by these figures, day-to-day bias errors in estimated source rate correlate highly with the errors in the modelled 3-m wind speed ($\rho = 0.974$), implying that source rate bias on a day-to-day basis is driven by error in the windspeed. By contrast, source rate and wind speed bias are negligibly correlated on a site-by-site basis ($\rho = 0.048$). This implies that site-specific sources of bias like surface albedo and site infrastructure that affects wind speed error are likely unimportant relative to day-to-day variability in wind speed error.

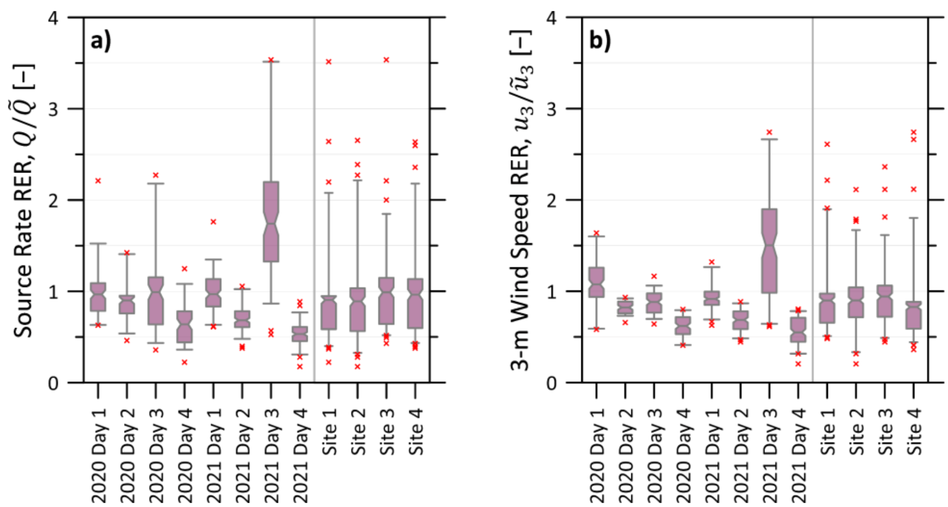

Figure 4: Box-whisker diagrams for the relative error ratio (RER) of source rate using Bridger's estimates with Meteoblue wind data, accumulated by measurement day (a) and site (b). The central bars of the box-whisker diagrams are notched at the mean error (i.e., bias) and span the interquartile range; whiskers correspond to the 90% equal tail confidence interval (CI) and red crosses mark extreme data outside the 90% CI. Day-to-day variability is significant with bias errors ranging from 0.53 to 1.74.

Thus, while Eq. (6) is the only practical error model when constrained by limited controlled released data, Eq. (5) is preferred to avoid underestimation of uncertainties given the potential significance of day-to-day variability in measurement bias. The difference between these approaches is demonstrated in Figure 3c, where the present controlled release data for Bridger's GML from four sites over eight unique days in two different years is sufficient to model uncertainties via either Eq. (5) or (6). Use of Eq. (5) in place of the simplified Eq. (6) yielded no meaningful effect on the average bias, which changed less than 1%. However, as shown in the figure, and expected given the proper consideration of bias variability, Eq. (5) estimates higher dispersion in source rate RER (15% increase in standard deviation) than Eq. (6). This increased variability when considering day- and site-dependent bias is moderate but not insignificant, and implies an underestimation of quantification uncertainty if controlled release data are limited to a small number of locations and/or measurement days and Eq. (6) is used for quantification error analysis. Based on these results, it is highly recommended that future controlled release studies be completed from a range of unique locations and over as many different days as feasible.

5 Conclusions

Generalized models to characterize probabilities of detection and quantification error were developed and applied to three aerial methane-detection technologies: Bridger Photonics Inc.'s Gas-Mapping LiDAR (GML), Kairos Aerospace's LeakSurveyor, and the (U.S.) National Aeronautic and Space Administration's Jet Propulsion Laboratory's Next-Generation Airborne Visible/Infrared Imaging Spectrometer (AVIRIS-NG). Leveraging binary regression with a generalized predictor function, this new method improves upon existing techniques in the literature by enabling derivation of continuous and physically realizable POD functions that are variable on methane source rate, ambient wind speed, and aircraft altitude (where available). POD functions optimized to available controlled release data identified technology-specific detection sensitivities that vary with wind speed and altitude. At typical/target aircraft altitudes and a representative average wind speed of 3 m/s, Bridger's GML, Kairos' LeakSurveyor, and AVIRIS-NG were predicted to identify methane emissions of 1.2, 27, and 6.0 kg/h with 50% probability, respectively.

Using a subset of controlled release data for Bridger's GML and Kairos' LeakSurveyor that included source rate estimates for comparison with ground truth controlled source rates, quantification uncertainties were separately characterized, including analysis of effects of using four optional database sources of wind speed for Kairos' LeakSurveyor. The developed statistical model permits analysis of measurement bias, *variability* in measurement bias (where data permitted), and measurement precision, where the latter two were treated as probabilistic variables. Using the Meteoblue wind speed data product, the source rate relative error ratio (RER – i.e., controlled over estimated source rate) for Bridger's GML averaged to 0.95 with a 95% confidence interval of 0.35−2.41. The analysis of Kairos' LeakSurveyor identify that source rate RER was highly sensitive to the wind speed data source and statistic (i.e., gust vs. average wind speed) and gust wind speed provided significantly less-biased results. One-minute gust wind speed from the Dark Sky database and one-hour gust wind speed from the High-Resolution Rapid Refresh database yielded mean source rate RERs of 1.04 and 1.34 with 95% confidence intervals of 0.38–2.02 and 0.56–3.81, respectively. Data from the present controlled release study of Bridger's GML demonstrated that day-to-day variability in measurement bias was strongly correlated with wind speed error and appreciably increased the dispersion of the source rate RER. These results identify the need to target an assortment of different measurement locations and maximize measurement days during future controlled release studies.

Ultimately, the described methods – successfully applied to three example technologies – yield the robustly derived continuous POD function and probabilistic quantification error model that are needed to properly simulate emissions abatement/reduction and support methane monitoring, reporting, and verification via aircraft-based remote sensing. Moreover, the developed generalized methods are readily extensible to analysis of other remote sensing techniques or can be used to update POD and uncertainty models as further controlled release data become publicly available.

Funding

This work was supported by Natural Resources Canada (NRCan, grant number EIP2-MET-001), Natural Sciences and Engineering Research Council of Canada (grant numbers 06632 and 522658), Environment and Climate Change Canada (ECCC, contract number 300071420), and Environmental Defense Fund.

Declaration of Competing Interest

The authors have no competing interests to declare.

Acknowledgements

This project was possible only through the expertise of members of the Energy & Emissions Research Lab who participated in the 2020 and/or 2021 field experiments, including Scott Seymour, Simon Festa-Bianchet, Zachary Milani, Ellen McCole, Cameron Roth, Damon Burtt, Parvin Mehr, Milad Mohammadi, and Fraser Kirby with additional support from Brigid Bedard-Hinz, Alex Szekeres, and Reese Bartlett (GreenPath Energy Ltd.). The authors are especially grateful to Mark Anderson (Husky Energy Ltd.) for arranging site access to make the semi- and fully blinded release work possible and to Michael Layer and Nicole MacDonald (Natural Resources Canada), Don D'Souza (British Columbia Ministry of Environment and Climate Change Strategy), and James Diamond (Environment & Climate Change Canada) for their leadership in initiating this and related methane survey work in our lab. Finally, the support of BC Oil and Gas Methane Emissions Research Collaborative (MERC) in parallel work applying these results is gratefully acknowledged.

Supplementary Information

Supplementary information to this article can be found online.

References

AER, 2021. Alternative Fugitive Emission Management Program Approvals [WWW Document]. URL https://www.aer.ca/protecting-what-matters/holding-industry-accountable/industry-performance/methane-performance/alternative-fugitive-emission-management-program-approvals (accessed 2.15.21).

Apple Inc., 2022. Dark Sky API [WWW Document]. URL https://darksky.net/dev (accessed 6.9.22).

Arias, P.A., Bellouin, N., Coppola, E., Jones, R.G., Krinner, G., Marotzke, J., Naik, V., Palmer, M.D., Plattner, G.-K., Rogelj, J., Rojas, M., Sillmann, J., Storelvmo, T., Thorne, P.W., Trewin, B., Rao, K.A., Adhikary, B., Allan, R.P., Armour, K., Bala, G., Barimalala, R., Berger, S., Canadell, J.G., Cassou, C., Cherchi, A., Collins, W., Collins, W.D., Connors, S.L., Corti, S., Cruz, F., Dentener, F.J., Dereczynski, C., Luca, A. Di, Niang, A.D., Doblas-Reyes, F.J., Dosio, A., Douville, H., Engelbrecht, F., Eyring, V., Fischer, E., Forster, P., Fox-Kemper, B., Fuglestvedt, J.S., Fyfe, J.C., Gillett, N.P., Goldfarb, L., Gorodetskaya, I., Gutierrez, J.M., Hamdi, R., Hawkins, E., Hewitt, H.T., Hope, P., Islam, A.S., Jones, C., Kaufman, D.S., Kopp, R.E., Kosaka, Y., Kossin, J., Krakovska, S., Lee, J.-Y., Li, J., Mauritsen, T., Maycock, T.K., Meinshausen, M., Min, S.-K., Monteiro, P.M.S., Ngo-Duc, T., Otto, F., Pinto, I., Pirani, A., Raghavan, K., Ranasinghe, R., Ruane, A.C., Ruiz, L., Sallée, J.-B., Samset, B.H., Sathyendranath, S., Seneviratne, S.I., Sörensson, A.A., Szopa, S., Takayabu, I., A.-M.Tréguier, Hurk, B. van den, R.Vautard, Schuckmann, K. von, Zaehle, S., Zhang, X., Zickfeld, K., 2021. Technical Summary, in: Masson-Delmott, V., Zhai, P., Pirani, A., Connors, S.L., Péan, C., Berger, S., Caud, N., Chen, Y., Goldfarb, L., Gomis, M.I., Huang, M., Leitzell, K., Lonnoy, E., Matthews, J.B.R., Maycock, T.K., Waterfield, T., Yelekçi, O., Yu, R., Zhoue, B. (Eds.), Climate Change 2021: The Physical Science Basis. Contribution of Working Group I to the Sixth Assessment Report of the Intergovernmental Panel on Climate Change. Cambridge University Press, pp. 33–144. https://doi.org/10.1017/9781009157896.002

ARPA-E, 2018. Impact Sheet - Bridger Photonics (MONITOR) [WWW Document]. URL https://arpa-e.energy.gov/impact-sheet/bridger-photonics-monitor (accessed 5.23.22).

Bell, C., Vaughn, T.L., Zimmerle, D.J., 2020. Evaluation of next generation emission measurement technologies under repeatable test protocols. Elem Sci Anth 8, 32. https://doi.org/10.1525/elementa.426

Berman, E., S.F., W., B., E., Jones, B.B., 2021. Kairos Aerospace Technical White Paper: Methane Detection (Version 1F). Kairos Aerospace. https://doi.org/10.17605/OSF.IO/HZG52

Branson, K., Jones, B.B., Berman, E.S.F., 2021. Methane Emissions Quantification (No. Version 2). Kairos Aerospace, Mountain Vew, CA.

Bridger Photonics, 2022. Gas Mapping LiDAR gains regulatory approval for ALARM use in New Mexico [WWW Document]. URL https://www.bridgerphotonics.com/blog/gas-mapping-lidar-gains-regulatory-approval-alarm-use-new-mexico (accessed 5.23.22).

Bridger Photonics, 2021. Gas Mapping LiDAR™ [WWW Document]. URL https://www.bridgerphotonics.com/gas-mapping-lidar (accessed 5.31.21).

CCAC, 2021. Global Methane Pledge [WWW Document]. URL https://www.globalmethanepledge.org/ (accessed 4.28.22).

Chen, Y., Sherwin, E.D., Berman, E.S.F., Jones, B.B., Gordon, M.P., Wetherley, E.B., Kort, E.A., Brandt, A.R., 2022. Quantifying Regional Methane Emissions in the New Mexico Permian Basin with a Comprehensive Aerial Survey, Environmental Science & Technology. https://doi.org/10.1021/acs.est.1c06458

Cusworth, D.H., Duren, R.M., Thorpe, A.K., Olson-Duvall, W., Heckler, J., Chapman, J.W., Eastwood, M.L., Helmlinger, M.C., Green, R.O., Asner, G.P., Dennison, P.E., Miller, C.E., 2021. Intermittency of Large Methane Emitters in the Permian Basin. Environ. Sci. Technol. Lett. 8, 567–573. https://doi.org/10.1021/acs.estlett.1c00173

Cusworth, D.H., Duren, R.M., Thorpe, A.K., Tseng, E., Thompson, D., Guha, A., Newman, S., Foster, K.T., Miller, C.E., 2020. Using remote sensing to detect, validate, and quantify methane emissions from California solid waste operations. Environ. Res. Lett. 15. https://doi.org/10.1088/1748-9326/ab7b99

Duren, R.M., Thorpe, A.K., Foster, K.T., Rafiq, T., Hopkins, F.M., Yadav, V., Bue, B.D., Thompson, D.R., Conley, S., Colombi, N.K., Frankenberg, C., McCubbin, I.B., Eastwood, M.L., Falk, M., Herner, J.D., Croes, B.E., Green, R.O., Miller, C.E., 2019. California's methane super-emitters. Nature 575, 180–184. https://doi.org/10.1038/s41586-019-1720-3

Elder, C.D., Thompson, D.R., Thorpe, A.K., Hanke, P., Walter Anthony, K.M., Miller, C.E., 2020. Airborne Mapping Reveals Emergent Power Law of Arctic Methane Emissions. Geophys. Res. Lett. 47. https://doi.org/10.1029/2019GL085707

European Commission, 2021. Proposal for a Regulation of the European Parliament and of the Council on methane emissions reduction in the energy sector and amending Regulation (EU) 2019/942. European Commission, Brussels.

Foote, M.D., Dennison, P.E., Thorpe, A.K., Thompson, D.R., Jongaramrungruang, S., Frankenberg, C., Joshi, S.C., 2020. Fast and Accurate Retrieval of Methane Concentration From Imaging Spectrometer Data Using Sparsity Prior. IEEE Trans. Geosci. Remote Sens. 58, 6480–6492. https://doi.org/10.1109/TGRS.2020.2976888

Fox, T.A., Barchyn, T.E., Risk, D., Ravikumar, A.P., Hugenholtz, C.H., 2019. A review of close-range and screening technologies for mitigating fugitive methane emissions in upstream oil and gas. Environ. Res. Lett. 14, 053002. https://doi.org/10.1088/1748-9326/ab0cc3

Frankenberg, C., Thorpe, A.K., Thompson, D.R., Hulley, G., Kort, E.A., Vance, N., Borchardt, J., Krings, T., Gerilowski, K., Sweeney, C., Conley, S.A., Bue, B.D., Aubrey, A.D., Hook, S., Green, R.O., 2016. Airborne methane remote measurements reveal heavytail flux distribution in Four Corners region. Proc. Natl. Acad. Sci. U. S. A. 113, 9734–9739. https://doi.org/10.1073/pnas.1605617113

Green, R.O., Eastwood, M.L., Sarture, C.M., Chrien, T.G., Aronsson, M., Chippendale, B.J., Faust, J.A., Pavri, B.E., Chovit, C.J., Solis, M., Olah, M.R., Williams, O., 1998. Imaging Spectroscopy and the Airborne Visible/Infrared Imaging Spectrometer (AVIRIS). Remote Sens. Environ. 65, 227–248. https://doi.org/10.1016/S0034-4257(98)00064-9

Guha, A., Newman, S., Fairley, D., Dinh, T.M., Duca, L., Conley, S.C., Smith, M.L., Thorpe, A.K., Duren, R.M., Cusworth, D.H., Foster, K.T., Fischer, M.L., Jeong, S., Yesiller, N., Hanson, J.L., Martien, P.T., 2020. Assessment of Regional Methane Emission Inventories through Airborne Quantification in the San Francisco Bay Area. Environ. Sci. Technol. 54, 9254–9264. https://doi.org/10.1021/acs.est.0c01212

Hamlin, L., Green, R.O., Mouroulis, P., Eastwood, M., Wilson, D., Dudik, M., Paine, C., 2011. Imaging spectrometer science measurements for Terrestrial Ecology: AVIRIS and new developments, in: 2011 Aerospace Conference. IEEE, pp. 1–7. https://doi.org/10.1109/AERO.2011.5747395

Hanna, S.R., Briggs, G.A., Hosker Jr., R.P., 1982. Handbook on atmospheric diffusion.

Hunter, D., Thorpe, M.J., 2017. Gas Mapping LiDAR Aerial Verification Program Final Report. Alberta Upstream Petroleum Research Fund Project 17-ARPC-03, Petroleum Technology Alliance of Canada (PTAC).

InvestableUniverse, 2021. Breakthrough For LiDAR Tech In Oil And Gas Industry After Exxon Filing [WWW Document]. URL https://investableuniverse.com/2021/04/09/bridger-photonics-lidar-methane-emissions-exxon-mobil/ (accessed 5.23.22).

IPCC, 2018. Summary for Policymakers, in: Masson-Delmotte, V., Zhai, P., Pörtner, H.-O., Roberts, D., Skea, J., Shukla, P.R., Pirani, A., Moufouma-Okia, W., Péan, C., Pidcock, R., Connors, S., Matthews, J.B.R., Chen, Y., Zhou, X., Gomis, M.I., Lonnoy, E., Maycock, T., Tignor, M., Waterfield, T. (Eds.), Global Warming of 1.5°C. An IPCC Special Report on the Impacts of Global Warming of 1.5°C above Pre-Industrial Levels. Intergovernmental Panel on Climate Change.

Jervis, D., McKeever, J., Durak, B.O.A., Sloan, J.J., Gains, D., Varon, D.J., Ramier, A., Strupler, M., Tarrant, E., 2021. The GHGSat-D imaging spectrometer. Atmos. Meas. Tech. 14, 2127–2140. https://doi.org/10.5194/amt-14-2127-2021

Johnson, M.R., Tyner, D.R., Szekeres, A.J., 2021. Blinded evaluation of airborne methane source detection using Bridger Photonics LiDAR. Remote Sens. Environ. 259, 112418. https://doi.org/10.1016/j.rse.2021.112418

Kairos Aerospace, 2022a. New Mexico Authority Approves Kairos Aerospace Technology in Methane Emissions Mitigation Efforts [WWW Document]. URL https://kairosaerospace.com/new-mexico-authority-approves-kairos-aerospace-technology-in-methane-emissions-mitigation-efforts/ (accessed 6.2.22).

Kairos Aerospace, 2022b. Methane Detection from a Unique Perspective [WWW Document]. URL https://kairosaerospace.com/methane-detection/ (accessed 5.29.22).

Kass, R.E., Raftery, A.E., 1995. Bayes Factors. J. Am. Stat. Assoc. 90, 773–795.

Kemp, C.E., Ravikumar, A.P., 2021. New Technologies Can Cost Effectively Reduce Oil and Gas Methane Emissions, but Policies Will Require Careful Design to Establish Mitigation Equivalence. Environ. Sci. Technol. 55, 9140–9149. https://doi.org/10.1021/acs.est.1c03071

Kemp, C.E., Ravikumar, A.P., Brandt, A.R., 2016. Comparing Natural Gas Leakage Detection Technologies Using an Open-Source “virtual Gas Field” Simulator. Environ. Sci. Technol. 50, 4546–4553. https://doi.org/10.1021/acs.est.5b06068

Krautwurst, S., Gerilowski, K., Jonsson, H.H., Thompson, D.R., Kolyer, R.W., Iraci, L.T., Thorpe, A.K., Horstjann, M., Eastwood, M., Leifer, I., Vigil, S.A., Krings, T., Borchardt, J., Buchwitz, M., Fladeland, M.M., Burrows, J.P., Bovensmann, H., 2017. Methane emissions from a Californian landfill, determined from airborne remote sensing and in situ measurements. Atmos. Meas. Tech. 10, 3429–3452. https://doi.org/10.5194/amt-10-3429-2017

Kreitinge, A.T., Thorpe, M.J., 2018. High-Sensitivity Gas-Mapping 3D Imager and Method of Operation. 9970756 B2.

NOAA, 2020. High-Resolution Rapid Refresh (HRRR) Model [WWW Document]. URL https://rapidrefresh.noaa.gov/ (accessed 6.9.22).

Rashid, K., Speck, A., Osedach, T.P., Perroni, D. V., Pomerantz, A.E., 2020. Optimized inspection of upstream oil and gas methane emissions using airborne LiDAR surveillance. Appl. Energy 275, 115327. https://doi.org/10.1016/j.apenergy.2020.115327

Ravikumar, A.P., Sreedhara, S., Wang, J., Englander, J.G., Roda-Stuart, D., Bell, C.S., Zimmerle, D.J., Lyon, D.R., Mogstad, I., Ratner, B., Brandt, A.R., 2019. Single-blind inter-comparison of methane detection technologies – results from the Stanford/EDF Mobile Monitoring Challenge. Elem Sci Anth 7, 37. https://doi.org/10.1525/elementa.373

Schwietzke, S., Harrison, M., Lauderdale, T., Branson, K., Conley, S.A., George, F.C., Jordan, D., Jersey, G.R., Zhang, C., Mairs, H.L., Pétron, G., Schnell, R.C., 2019. Aerially guided leak detection and repair: A pilot field study for evaluating the potential of methane emission detection and cost-effectiveness. J. Air Waste Manag. Assoc. 69, 71–88. https://doi.org/10.1080/10962247.2018.1515123

Sherwin, E.D., Chen, Y., Ravikumar, A.P., Brandt, A.R., 2021. Single-blind test of airplane-based hyperspectral methane detection via controlled releases. Elem. Sci. Anthr. 9. https://doi.org/10.1525/elementa.2021.00063

Snipes, M., Taylor, D.C., 2014. Model selection and Akaike Information Criteria: An example from wine ratings and prices. Wine Econ. Policy 3, 3–9. https://doi.org/10.1016/j.wep.2014.03.001

Thompson, D.R., Leifer, I., Bovensmann, H., Eastwood, M., Fladeland, M., Frankenberg, C., Gerilowski, K., Green, R.O., Kratwurst, S., Krings, T., Luna, B., Thorpe, A.K., 2015. Real-time remote detection and measurement for airborne imaging spectroscopy: a case study with methane. Atmos. Meas. Tech. 8, 4383–4397. https://doi.org/10.5194/amt-8-4383-2015

Thorpe, A.K., Duren, R.M., Conley, S., Prasad, K.R., Bue, B.D., Yadav, V., Foster, K.T., Rafiq, T., Hopkins, F.M., Smith, M.L., Fischer, M.L., Thompson, D.R., Frankenberg, C., McCubbin, I.B., Eastwood, M.L., Green, R.O., Miller, C.E., 2020. Methane emissions from underground gas storage in California. Environ. Res. Lett. 15, 045005. https://doi.org/10.1088/1748-9326/ab751d

Thorpe, A.K., Frankenberg, C., Aubrey, A.D., Roberts, D.A., Nottrott, A.A., Rahn, T.A., Sauer, J.A., Dubey, M.K., Costigan, K.R., Arata, C., Steffke, A.M., Hills, S., Haselwimmer, C., Charlesworth, D., Funk, C.C., Green, R.O., Lundeen, S.R., Boardman, J.W., Eastwood, M.L., Sarture, C.M., Nolte, S.H., Mccubbin, I.B., Thompson, D.R., McFadden, J.P., 2016. Mapping methane concentrations from a controlled release experiment using the next generation airborne visible/infrared imaging spectrometer (AVIRIS-NG). Remote Sens. Environ. 179, 104–115. https://doi.org/10.1016/j.rse.2016.03.032

Tyner, D.R., Johnson, M.R., 2021. Where the Methane Is—Insights from Novel Airborne LiDAR Measurements Combined with Ground Survey Data. Environ. Sci. Technol. 55, 9773–9783. https://doi.org/10.1021/acs.est.1c01572

Varon, D.J., Jacob, D.J., Jervis, D., McKeever, J., 2020. Quantifying Time-Averaged Methane Emissions from Individual Coal Mine Vents with GHGSat-D Satellite Observations. Environ. Sci. Technol. 54, 10246–10253. https://doi.org/10.1021/acs.est.0c01213

Varon, D.J., Jacob, D.J., McKeever, J., Jervis, D., Durak, B.O.A., Xia, Y., Huang, Y., 2018. Quantifying methane point sources from fine-scale satellite observations of atmospheric methane plumes. Atmos. Meas. Tech. 11, 5673–5686. https://doi.org/10.5194/amt-11-5673-2018

Supplemental Information

Robust Probabilities of Detection and Quantification Uncertainty for Aerial Methane Detection: Examples for Three Airborne Technologies

Bradley M. Conrad, David R. Tyner, Matthew R. Johnson*

Energy & Emissions Research Laboratory,
Department of Mechanical and Aerospace Engineering,
Carleton University, Ottawa, ON, Canada, K1S 5B6

*Corresponding author: Matthew.Johnson@carleton.ca

S1 Facilities for High-Flowrate Controlled Release Experiments of Bridger Photonics Inc.'s Gas-Mapping LiDAR

High-flowrate, controlled release experiments were completed to support the present analysis of quantification error for Bridger Photonic Inc.'s Gas-Mapping LiDAR (GML) technology. Expanding on the description in the main text, these were performed at four inactive oil and gas facilities (approximate GPS coordinates: 53.12°N, 109.65°W) located in Western Saskatchewan, Canada and shown in Figure S1. These previously oil-producing facilities were approximately 30 km southeast of the town of Lloydminster and each less than 100 m in size in the north-south direction such that they were easily captured in a single swath of Bridger's GML, mounted on an aircraft flying approximately west/eastward. The facilities were sufficiently spaced (approximately 350, 390, and 410 m apart from west to east) to avoid overlap of controlled release plumes granting Bridger the opportunity to measure four controlled releases in quick succession (<30 s at typical flight speeds). The aircraft looped over the facilities approximately every 4 minutes, permitting the ground teams to adjust controlled release rate (semi-blindly) between passes and ensuring detectable plumes from the previous pass were sufficiently dispersed and the new plumes had time to establish.

Figure S1: Four inactive, previously oil-producing, facilities used for high-flowrate controlled releases to study Bridger Photonics Inc.'s Gas-Mapping LiDAR technology. The four facilities were approximately 375 m apart in the west-east direction and less than 100 m in size in the north-south direction, permitting measurement of four controlled releases in rapid succession.

S2 Model Optimization and Selection

This section describes the model optimization and selection procedure for the derived probability of detection (POD) functions $\left(POD(\boldsymbol{x})\right)$ and quantification error distributions $\left(\pi\left(Q\middle|\tilde{Q}\right)\right)$.

The methodology to derive POD functions for a given measurement technology combines a predictor function ($g(\boldsymbol{x};\boldsymbol{\phi})$), which is variable on measured parameters and conditions ($\boldsymbol{x}$) and parameterized by $\boldsymbol{\phi}$**,** and an inverse link function ($F(g;\boldsymbol{\theta})$), which is variable on the predictor function output and is parameterized by $\boldsymbol{\theta}$. As discussed in the manuscript, a generalized predictor function of seven optional coefficients was used (Eq. (7)) in the manuscript and repeated below for convenience) and candidate inverse link functions included cumulative distribution functions (CDFs) of probability distributions with non-negative support. To avoid over-determination of this optimization problem, the coefficients of the candidate inverse link functions ($\boldsymbol{\theta}$) were constrained such that the distribution represented by the candidate CDF had a unit mean and unit variance. Eight probability distributions were considered for the inverse link function including the Burr Type XII, Fréchet, Gamma, and Log-logistic distributions. The candidate model that minimizes the corrected Akaike Information Criterion (AICc; Akaike, 1974) was deemed optimal.

$$g(\boldsymbol{x};\boldsymbol{\phi}) = \phi_7 \frac{\left(Q_{[\mathrm{kg/h}]} - \phi_1\right)^{\phi_3}}{\tilde{n}_{[\mathrm{ppm\cdot m}]}^{\phi_4} \left(\frac{h_{[\mathrm{m}]}}{1000}\right)^{\phi_5} \left(u_{3[\mathrm{m/s}]} - \phi_2\right)^{\phi_6}} \tag{7}$$

Referring to the predictor function (Eq. (7)) and discussion in the manuscript, coefficients could be optionally fixed to ignore the effect of, for example, scene noise or aircraft altitude on detection probability. With the present controlled release data for Bridger's GML, for which a subset included scene noise data, the importance of each coefficient was studied. Firstly, if coefficients ϕ_1 and ϕ_2 were optimized (such that $\phi_1 \geq 0$ and $\phi_2 \leq 0$), the optimum was obtained when ϕ_1 was approximately zero; this was consistent across technologies, where the optimized $\phi_1 = 0$ throughout. After this observation, the relative importance of scene noise and aircraft altitude was assessed by optionally fixing ϕ_4 and/or ϕ_5 to zero and optimizing the POD for the subset of Bridger GML data where scene noise was available (N = 178). The marginal benefit of including an additional non-fixed coefficient (i.e., ϕ_4 and/or ϕ_5) was assessed using the AICc. This parameter, technically a "Bayes Factor" (e.g., Snipes and Taylor, 2014), is used to quantify the relative goodness of models and is a function of the optimized value of the negative log-likelihood function (i.e., the objective function of the optimization) and with a penalty on number of optimized variables. The difference in the AICc (ΔAICc) between an *initial model* and an *alternative model* is indicative of the statistical justification for the latter over the former. This result is typically interpreted using Kass and Raftery's (1995) classification, where ΔAICc in (0, $10^{0.5}$) implies that the difference between models is "not worth more than a bare mention" and ΔAICc in ($10^{0.5}$, 10^1) and (10^1, 10^2) imply that there is "substantial" and "strong" justification for the alternative model over the initial model. As summarized in Table S1 and discussed in the manuscript, the consideration of scene noise *or* aircraft altitude is strongly justified (ΔAICc ≈ $10^{1.25}$). By contrast, the marginal benefit of including noise or aircraft altitude if the other is already in the initial model is much weaker, cusping the "not worth more than a bare mention" classification.

Table S1: Summary of goodness-of-fit statistics for models that incrementally include consideration of representative scene noise or aircraft altitude.

Initial Model:		**Alternative Model:**		**Average ΔAICc of Eight Candidate Models**
Noise	Altitude	Noise	Altitude	
No	No	No	Yes	$10^{1.25}$
No	No	Yes	No	$10^{1.25}$
No	Yes	Yes	Yes	$10^{0.51}$
Yes	No	Yes	Yes	$10^{0.50}$

Coefficients ($\boldsymbol{\phi}$) of the optimized predictor function $\left(g(\boldsymbol{x}; \boldsymbol{\phi})\right)$ are shown in Table S2 for each technology: Bridger Photonics Inc.'s Gas-Mapping LiDAR (GML), Kairos Aerospace's

LeakSurveyor, and AVIRIS-NG (Next-Generation Airborne Visible/Infrared Imaging Spectrometer) from the (U.S.) National Aeronautics and Space Administration's (NASA's) Jet Propulsion Laboratory (JPL). Table S3 additionally provides the complete equations for these predictor functions as well as the inverse link functions $\left(F(g;\boldsymbol{\theta})\right)$; the composition of these equations yields the POD function $\left(POD(\boldsymbol{x})\right)$ for each technique, which are detailed in the final column of the table.

Table S2: Optimized coefficients of the predictor function $\left(g(x;\boldsymbol{\phi})\right)$ for each measurement technology.

Function/ Coefficient		**Bridger GML**	**Kairos LeakSurveyor**		**NASA JPL AVIRIS-NG**	
			without partial detections	**with partial detections**	**without partial detections**	**with partial detections**
Predictor function (g)	ϕ_1	0	0	0	0	0
	ϕ_2	1.072	2.054	2.027	2.431	1.101
	ϕ_3	–2.139	–0.929	–0.07006	–36.44	–37.11
	ϕ_4	0	—	—	—	—
	ϕ_5	2.440	—	—	0.1.684	0.7343
	ϕ_6	1.692	2.056	1.527	7.643	4.420
	ϕ_7	0.1518	$13.35{\times}10^{-3}$	$5.363{\times}10^{-3}$	$14.23{\times}10^{9}$	$2.125{\times}10^{6}$

Modelling of the quantification error distributions was performed via Eq. (5) and (6) in the manuscript depending on the assumed (in)dependence of measurement bias with measurement date and location. Regardless of the assumption, model optimization and selection were performed using the AICc, like the model optimization/selection for POD. Table S4 summarizes the results for the quantification error analysis of Bridger's GML and Kairos' LeakSurveyor. The optimized bias-correction functions $\left(\hat{Q} = f_B\left(\tilde{Q}\right)\right)$ and bias- and precision-distributions (π_{κ_Q} and π_{λ_Q} as needed, where $\kappa_Q = Q/\tilde{Q}$ and $\lambda_Q = Q/\hat{Q}$) are shown for each of the technologies and wind data sources discussed in the manuscript. These results are combined in the last column of the table to yield the conditional distribution for quantification error, $\pi\left(Q\middle|\tilde{Q}\right)$. Table S5 summarizes the same analysis for wind speed error distributions, $\pi(u_3|\tilde{u}_3)$ to support calcultions via Eq. (10) in the main text.

Table S3: Detailed equations for the predictor, inverse link, and composite POD functions for each measurement technology.

Instrument	**Predictor Function** $g(Q, u_3, \tilde{h})$	**Inverse Link Function** $F(g)$	**Detailed Equation for** $\mathrm{POD}(Q, u_3, \tilde{h})$
Bridger Photonics Inc. GML	$\dfrac{0.1518\, Q_{[\mathrm{kg/h}]}^{1.072}}{\left(\dfrac{\tilde{h}_{[\mathrm{m}]}}{1000}\right)^{2.440} \left(u_{3[\mathrm{m/s}]} + 2.139\right)^{1.692}}$	Fréchet CDF: $\exp(-0.3719 g^{-2.530})$	$\exp\left(-\left(\dfrac{0.2244\, Q_{[\mathrm{kg/h}]}^{1.072}}{\left(\dfrac{\tilde{h}_{[\mathrm{m}]}}{1000}\right)^{2.440} \left(u_{3[\mathrm{m/s}]} + 2.139\right)^{1.692}}\right)^{-2.530}\right)$
Kairos Aerospace LeakSurveyor[a]	$\dfrac{(13.35 \times 10^{-3})\, Q_{[\mathrm{kg/h}]}^{2.054}}{\left(u_{3[\mathrm{m/s}]} + 0.9296\right)^{2.056}}$	Burr Type XII CDF: $1 - (1 + 0.2976 g^{1.303})^{-3.906}$	$1 - \left(1 + \left(\dfrac{(5.266 \times 10^{-3})\, Q_{[\mathrm{kg/h}]}^{2.054}}{\left(u_{3[\mathrm{m/s}]} + 0.9296\right)^{2.056}}\right)^{1.303}\right)^{-3.906}$
Including Partial Detections	$\dfrac{(5.363 \times 10^{-3})\, Q_{[\mathrm{kg/h}]}^{2.027}}{\left(u_{3[\mathrm{m/s}]} + 0.07006\right)^{1.527}}$	Burr Type XII CDF: $1 - (1 + 0.2976 g^{1.303})^{-3.906}$	$1 - \left(1 + \left(\dfrac{(2.116 \times 10^{-3})\, Q_{[\mathrm{kg/h}]}^{2.027}}{\left(u_{3[\mathrm{m/s}]} + 0.07006\right)^{1.527}}\right)^{1.303}\right)^{-3.906}$
AVIRIS-NG	$\dfrac{(14.23 \times 10^{9})\, Q_{[\mathrm{kg/h}]}^{2.431}}{\left(\dfrac{\tilde{h}_{[\mathrm{m}]}}{1000}\right)^{1.684} \left(u_{3[\mathrm{m/s}]} + 36.44\right)^{7.643}}$	Burr Type XII CDF: $1 - (1 + 0.2976 g^{1.303})^{-3.906}$	$1 - \left(1 + \left(\dfrac{(5.613 \times 10^{9})\, Q_{[\mathrm{kg/h}]}^{2.431}}{\left(\dfrac{\tilde{h}_{[\mathrm{m}]}}{1000}\right)^{1.684} \left(u_{3[\mathrm{m/s}]} + 36.44\right)^{7.643}}\right)^{1.303}\right)^{-3.906}$
Including Partial Detections	$\dfrac{(2.125 \times 10^{6})\, Q_{[\mathrm{kg/h}]}^{1.101}}{\left(\dfrac{\tilde{h}_{[\mathrm{m}]}}{1000}\right)^{0.7343} \left(u_{3[\mathrm{m/s}]} + 37.11\right)^{4.420}}$	Fréchet CDF: $\exp(-0.3719 g^{-2.530})$	$\exp\left(-\left(\dfrac{(3.141 \times 10^{6})\, Q_{[\mathrm{kg/h}]}^{1.101}}{\left(\dfrac{\tilde{h}_{[\mathrm{m}]}}{1000}\right)^{0.7343} \left(u_{3[\mathrm{m/s}]} + 37.11\right)^{4.420}}\right)^{-2.530}\right)$

[a] Result for Kairos' LeakSurveyor technology at fixed aircraft altitude of 900 m.

Table S4: Optimized bias-correction functions and precision distributions for estimated source rate using Bridger's GML and Kairos' LeakSurveyor technologies with various wind speed data. Optimized bias-correction functions were proportional models and precision-correction distributions took the form of various non-negative probability distributions with unit mean. Detailed equations for the resulting quantification error distribution $\left(\boldsymbol{\pi}(\boldsymbol{Q}\mid\tilde{\boldsymbol{Q}})\right)$ are also provided.

Instrument	Wind Source	Bias-correction Function $f_B(\tilde{Q}) = d\tilde{Q}$	Bias- and Precision-Correction Distributions[a] π_{κ_Q} and π_{λ_Q}	Detailed Equation for $\pi(Q\mid\tilde{Q})$
Bridger Photonics Inc. GML	Meteoblue – Proprietary averaging	$d = 0.948$	$\lambda_Q \sim Burr\left(\underbrace{0.743}_{\alpha},\underbrace{4.55}_{c},\underbrace{0.659}_{k}\right)$	$\frac{\frac{kc}{\alpha}\left(\frac{Q}{d\alpha\tilde{Q}}\right)^{c-1}}{d\tilde{Q}\left(1+\left(\frac{Q}{d\alpha\tilde{Q}}\right)^{c}\right)^{k+1}}$
Bridger Photonics Inc. GML[b]	Meteoblue – Proprietary averaging	$d = 0.939$	$\kappa_Q \sim LL\left(\underbrace{0.944}_{\alpha},\underbrace{5.36}_{\beta}\right)$ $\lambda_Q \sim Burr\left(\underbrace{0.752}_{\alpha},\underbrace{4.53}_{c},\underbrace{0.674}_{k}\right)$	$\pi(Q\mid\tilde{Q}) = \int_{\hat{Q}} \pi_{\lambda_Q}\left(\frac{Q}{\hat{Q}}\right)\pi_{\kappa_Q}\left(\frac{\hat{Q}}{f_B(\tilde{Q})}\right)\frac{1}{\hat{Q}f_B(\tilde{Q})}d\hat{Q}$
Kairos Aerospace LeakSurveyor	Dark Sky – 1-minute average	$d = 2.14$	$\lambda_Q \sim LL\left(\underbrace{0.930}_{\alpha},\underbrace{4.79}_{\beta}\right)$	$\frac{\left(\frac{\beta}{\alpha}\right)\left(\frac{Q}{d\alpha\tilde{Q}}\right)^{\beta-1}}{d\tilde{Q}\left(1+\left(\frac{Q}{d\alpha\tilde{Q}}\right)^{\beta}\right)^{2}}$
	Dark Sky – 1-minute gust[c]	$d = 1.04$	$\lambda_Q \sim \Gamma\left(\underbrace{5.93}_{\alpha},\underbrace{0.169}_{\beta}\right)$	$\frac{\left(d\tilde{Q}\beta\right)^{-\alpha}}{\Gamma(\alpha)}Q^{\alpha-1}\exp\left(-\frac{Q}{d\tilde{Q}\beta}\right)$
	HRRR – 1-hour average	$d = 2.53$	$\lambda_Q \sim GEV\left(\underbrace{0.489}_{k},\underbrace{0.282}_{\sigma},\underbrace{0.576}_{\mu}\right)$	$\frac{1}{d\sigma\tilde{Q}}\left(1+k\frac{\left(\frac{Q}{d\tilde{Q}}-\mu\right)}{\sigma}\right)^{-\frac{k+1}{k}}\exp\left(-\left(1+k\frac{\left(\frac{Q}{d\tilde{Q}}-\mu\right)}{\sigma}\right)^{-\frac{1}{k}}\right)$
	HRRR – 1-hour gust	$d = 1.34$	$\lambda_Q \sim GEV\left(\underbrace{0.386}_{k},\underbrace{0.265}_{\sigma},\underbrace{0.686}_{\mu}\right)$	

[a] Legend: *Burr* = Burr Type XII distribution; *Γ* = Gamma distribution. *GEV* = Generalized extreme value distribution; *LL* = Log-logistic distribution.
[b] Quantification error distribution fit to Bridger GML data assuming time- and location-dependent measurement bias (i.e., fit using Eq. (5) in the manuscript).
[c] Includes an additional 296 data from controlled release studies completed by Kairos.

Table S5: Optimized bias-correction functions and precision distributions for various 3-m wind speed data sources relevant to Bridger's GML and Kairos' LeakSurveyor technologies. Optimized bias-correction functions were proportional models and precision-correction distributions took the form of various non-negative probability distributions with unit mean. The detailed equations for the resulting quantification error distribution $\left(\boldsymbol{\pi}(\boldsymbol{u}_3 \mid \tilde{\boldsymbol{u}}_3)\right)$ are provided for use with Eq. (10) in the main text if seeking to derive POD functions that use modelled wind rather than in situ measured/actual wind.

Instrument	Wind Source	Bias-correction Function $f_B(\tilde{u}_3) = d\tilde{u}_3$	Bias- and Precision-Correction Distributions[a] $\pi_{\kappa_{u_3}}$ and $\pi_{\lambda_{u_3}}$	Detailed Equation for $\pi(u_3 \mid \tilde{u}_3)$
Bridger Photonics Inc. GML	Meteoblue – Proprietary averaging	$d = 0.906$	$\lambda_{u_3} \sim LL\left(\underbrace{0.903}_{\alpha}, \underbrace{4.05}_{\beta}\right)$	$\frac{\left(\frac{\beta}{\alpha}\right)\left(\frac{u_3}{d\alpha\tilde{u}_3}\right)^{\beta-1}}{d\tilde{u}_3\left(1+\left(\frac{u_3}{d\alpha\tilde{u}_3}\right)^{\beta}\right)^2}$
Bridger Photonics Inc. GML[b]	Meteoblue – Proprietary averaging	$d = 0.939$	$\kappa_{u_3} \sim IG\left(\underbrace{1}_{\mu}, \underbrace{10.6}_{\xi}\right)$ $\lambda_{u_3} \sim LL\left(\underbrace{0.904}_{\alpha}, \underbrace{4.08}_{\beta}\right)$	$\pi(u \mid \tilde{u}_3) = \int_{\hat{u}_3} \pi_{\lambda_{u_3}}\left(\frac{u_3}{\hat{u}_3}\right) \pi_{\kappa_{u_3}}\left(\frac{\hat{u}_3}{f_B(\tilde{u}_3)}\right) \frac{1}{\hat{u}_3 f_B(\tilde{u}_3)} d\hat{u}_3$
Kairos Aerospace LeakSurveyor	Dark Sky – 1-minute average	$d = 1.83$	$\lambda_{u_3} \sim LL\left(\underbrace{0.951}_{\alpha}, \underbrace{5.77}_{\beta}\right)$	$\frac{\left(\frac{\beta}{\alpha}\right)\left(\frac{u_3}{d\alpha\tilde{u}_3}\right)^{\beta-1}}{d\tilde{u}_3\left(1+\left(\frac{u_3}{d\alpha\tilde{u}_3}\right)^{\beta}\right)^2}$
	Dark Sky – 1-minute gust[c]	$d = 0.780$	$\lambda_{u_3} \sim W\left(\underbrace{1.11}_{\xi}, \underbrace{3.61}_{k}\right)$	$\frac{k}{d\xi\tilde{u}_3}\left(\frac{u_3}{d\xi\tilde{u}_3}\right)^{k-1} \exp\left(-\left(\frac{u_3}{d\xi\tilde{u}_3}\right)^{k}\right)$
	HRRR – 1-hour average	$d = 1.92$	$\lambda_{u_3} \sim IG\left(\underbrace{1}_{\mu}, \underbrace{2.80}_{\xi}\right)$	$\frac{1}{d\tilde{u}_3}\sqrt{\frac{\xi}{2\pi}\left(\frac{u_3}{d\tilde{u}_3}\right)^{-3}} \exp\left(-\frac{d\xi\tilde{u}_3\left(\frac{u_3}{d\tilde{u}_3}-1\right)^2}{2u_3}\right)$
	HRRR – 1-hour gust	$d = 1.05$	$\lambda_{u_3} \sim LL\left(\underbrace{0.908}_{\alpha}, \underbrace{4.18}_{\beta}\right)$	$\frac{\left(\frac{\beta}{\alpha}\right)\left(\frac{u_3}{d\alpha\tilde{u}_3}\right)^{\beta-1}}{d\tilde{u}_3\left(1+\left(\frac{u_3}{d\alpha\tilde{u}_3}\right)^{\beta}\right)^2}$

[a] Legend: *IG* = Inverse Gaussian distribution; *LL* = Log-logistic distribution; *W* = Weibull distribution.
[b] Quantification error distribution fit to Bridger GML data assuming time- and location-dependent measurement bias (i.e., fit using Eq. (5) in the manuscript).
[c] Includes an additional 296 data from controlled release studies completed by Kairos.

S3 Additional Detail of Data used in POD Derivations

The following figures support the discussion in the manuscript. Figure S2 plots available controlled release data for each measurement technology, the POD contours from the derived POD functions (replicated from the manuscript), and previously published detection sensitivities. Note that for each plot there are additional large-scale release data beyond the limits of the y-axis.

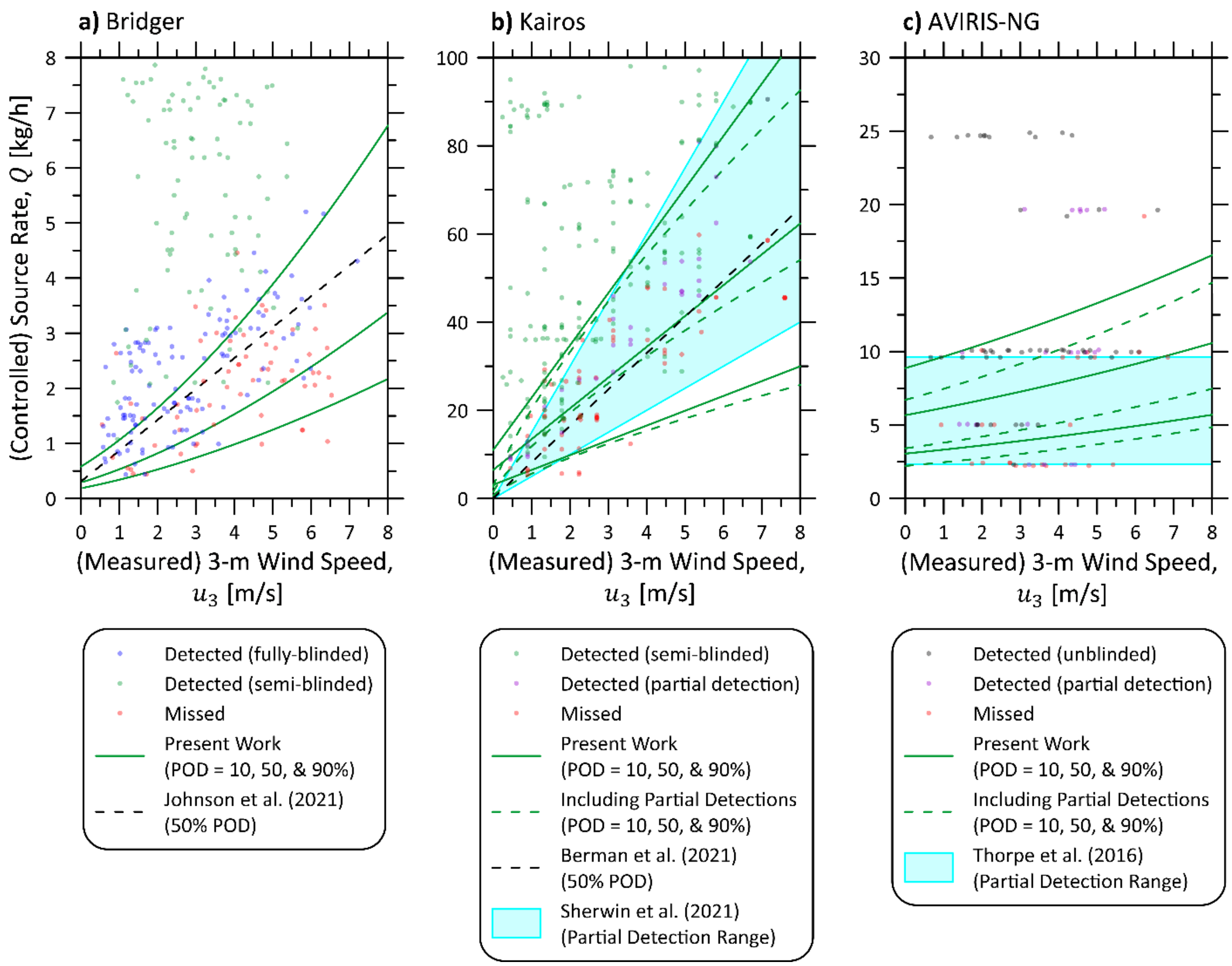

Figure S2: Comparison of probabilities of detections for Bridger's GML (a), Kairos' LeakSurveyor (b), and NASA JPL's AVIRIS-NG (c) technologies. Each figure plots probability contours using the present methodology (at 10, 50, and 90% POD) alongside available controlled release data which are coloured according to detection (black = unblinded, blue = fully blinded, green = semi-blinded) and miss (red). Each figure also identifies previously published estimates of detection sensitivity: 50% POD for Bridger's GML (Johnson et al., 2021) and Kairos' LeakSurveyor (Berman et al., 2021), and partial detection ranges for Kairos' LeakSurveyor (Sherwin et al., 2021) and NASA JPL's AVIRIS-NG (Thorpe et al., 2016).

Figure S3 provides the optimized POD function using the methodology in the present work and controlled release data for Kairos' LeakSurveyor. Subplots a) through c) show significant differences in the optimized POD when using Sherwin et al.'s (2021) data alone (a), Kairos' internal controlled release data alone (b), and the combination of these data sources (c).

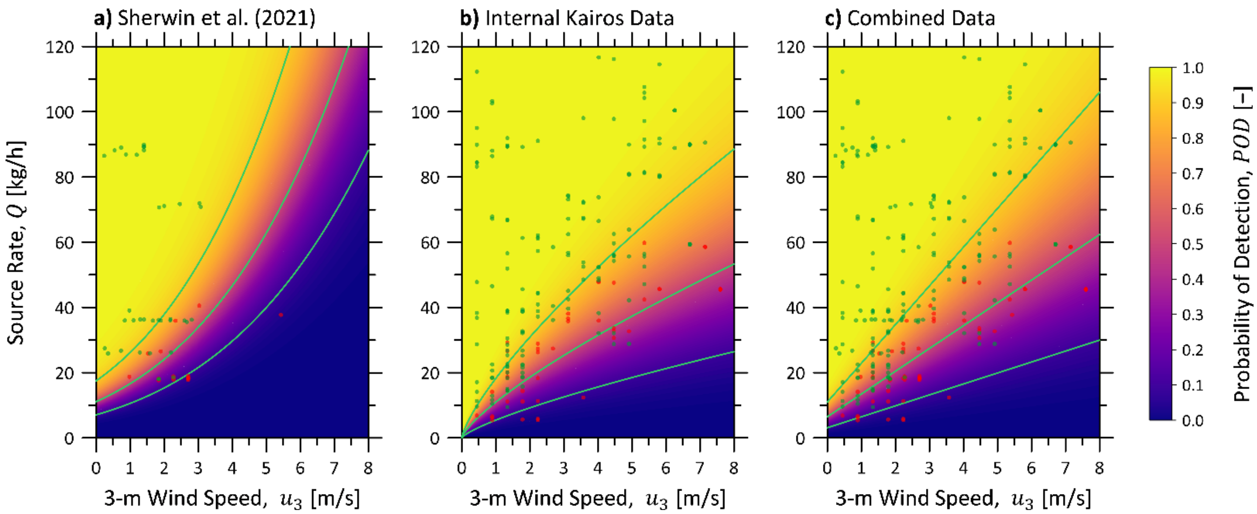

Figure S3: Optimized POD functions for Kairos' LeakSurveyor technology, ignoring partial detections using different data sets: a) the data of Sherwin et al. (2021) alone, b) the confidential data from Kairos' internal studies alone, and c) the combination of these data sources.

S4 References

Akaike, H., 1974. A new look at the statistical model identification. IEEE Transactions on Automatic Control 19, 716–723. https://doi.org/10.1109/TAC.1974.1100705

Berman, E., S.F., W., B., E., Jones, B.B., 2021. Kairos Aerospace Technical White Paper: Methane Detection (Version 1F). Kairos Aerospace. https://doi.org/10.17605/OSF.IO/HZG52

Johnson, M.R., Tyner, D.R., Szekeres, A.J., 2021. Blinded evaluation of airborne methane source detection using Bridger Photonics LiDAR. Remote Sensing of Environment 259, 112418. https://doi.org/10.1016/j.rse.2021.112418

Kass, R.E., Raftery, A.E., 1995. Bayes Factors. J Am Stat Assoc 90, 773–795.

Sherwin, E.D., Chen, Y., Ravikumar, A.P., Brandt, A.R., 2021. Single-blind test of airplane-based hyperspectral methane detection via controlled releases. Elementa: Science of the Anthropocene 9. https://doi.org/10.1525/elementa.2021.00063

Snipes, M., Taylor, D.C., 2014. Model selection and Akaike Information Criteria: An example from wine ratings and prices. Wine Economics and Policy 3, 3–9. https://doi.org/10.1016/j.wep.2014.03.001

Thorpe, A.K., Frankenberg, C., Aubrey, A.D., Roberts, D.A., Nottrott, A.A., Rahn, T.A., Sauer, J.A., Dubey, M.K., Costigan, K.R., Arata, C., Steffke, A.M., Hills, S., Haselwimmer, C., Charlesworth, D., Funk, C.C., Green, R.O., Lundeen, S.R., Boardman, J.W., Eastwood, M.L., Sarture, C.M., Nolte, S.H., Mccubbin, I.B., Thompson, D.R., McFadden, J.P., 2016. Mapping methane concentrations from a controlled release experiment using the next generation airborne visible/infrared imaging spectrometer (AVIRIS-NG). Remote Sensing of Environment 179, 104–115. https://doi.org/10.1016/j.rse.2016.03.032